J. Fluid Mech. (2022), *vol*. 935, A29, doi:10.1017/jfm.2021.625

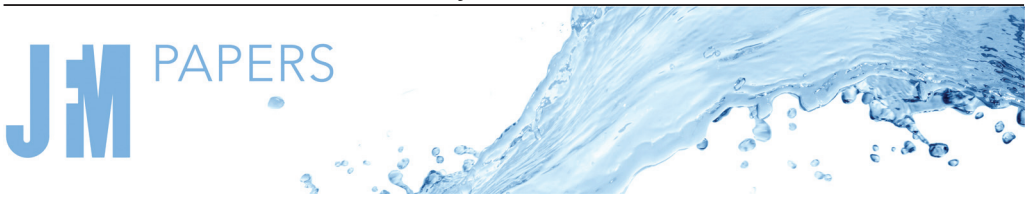

Mass, momentum and energy partitioning in unsteady fragmentation

Y. Wang[1] **and L. Bourouiba**[1],†

[1]The Fluid Dynamics of Disease Transmission Laboratory, Massachusetts Institute of Technology, Cambridge, MA 02139, USA

(Received 14 January 2020; revised 11 February 2021; accepted 2 July 2021)

Upon drop impact on a surface of comparable size to that of the drop, a sheet is produced that evolves freely in the air, bounded by a rim from which ligaments and droplets are continuously shed. This process is a canonical example of unsteady sheet fragmentation. The sheet dynamics is coupled with continuous ligament and drop shedding (Wang & Bourouiba, *J. Fluid Mech.*, vol. 848, 2018*b*, 946–967; Wang & Bourouiba, *J. Fluid Mech.*, vol. 910, 2021*b*, A39) and is governed by a nonlinear non-Galilean Taylor–Culick law (Wang & Bourouiba, 2022 (in press)). Here, we report the results of a combined theoretical and experimental study of the partition and temporal evolution of mass, momentum and energy in each part of the system composed of sheet, rim, ligaments and drops. We elucidate and derive analytical predictions, without fitting parameters, of the temporal evolution of the fractions of volume/mass, momentum and energy in each sub-part of the system: from sheet, to rim to fluid shed. We show that their temporal evolution and partitioning are independent of impact conditions. Interestingly this implies, for example, that the fraction of initial drop volume shed from an impacting drop is independent of the initial energy (or Weber number) of impact. We validate our predictions against precise measurements. Finally, we show that the partition laws for this unsteady fragmentation system are robust to changes of fluid properties (viscosity, surface tension and density). We provide the ranges of validity of our partition law on a Weber–Reynolds numbers regime map.

Key words: aerosols/atomization

1. Introduction

Fluid fragmentation selects the sizes of the emitted spray droplets (Rein 1993; Yarin 2006; Josserand & Thoroddsen 2016). An important class of sheet-mediated fragmentation systems in nature, industry and health are unsteady or require a transition through an unsteady state, where droplets are continuously generated with statistical properties that

† Email address for correspondence: lbouro@mit.edu

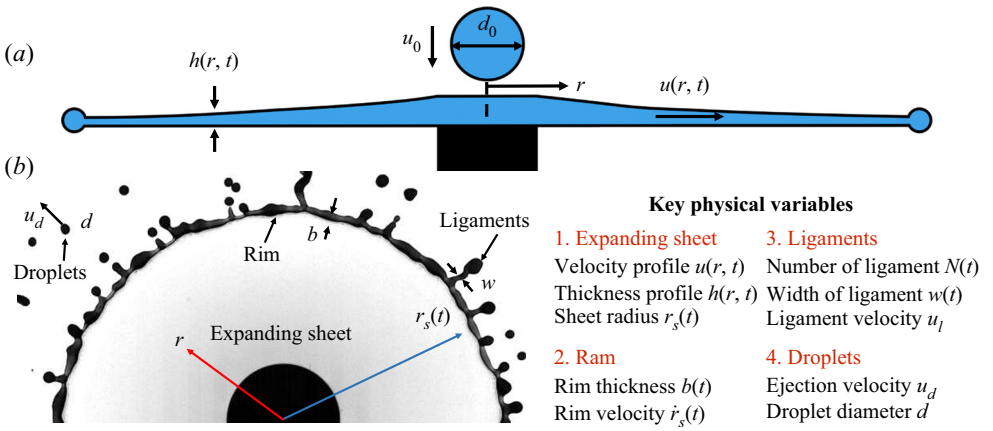

Figure 1. (*a*) Schematic diameter of canonical unsteady fragmentation upon drop impact on a rod of comparable size, d_r, to that of the impacting drop, d_0. (*b*) Snapshot of unsteady sheet upon drop impact on a rod with definition of key physical quantities of the fluid system involved.

vary over time (Wang & Bourouiba 2018*b*). This temporal variation governs the spray size and speed distributions, important for a range of applications involving the dispersal or deposition of chemical or biological compounds (Traverso *et al.* 2013; Bourouiba, Dehandschoewercker & Bush 2014; Gilet & Bourouiba 2014, 2015; Wang & Bourouiba 2018*a*; Bourouiba 2021*a*,*b*).

One canonical example of unsteady sheet fragmentation is that created from a drop impact, with diameter d_0, on a surface, or rod, of comparable size, d_r, to that of the drop. Such a phenomenon has been extensively studied in the literature (Rozhkov, Prunet-Foch & Vignes-Adler 2002, 2004; Villermaux & Bossa 2011; Vernay, Ramos & Ligoure 2015; Wang & Bourouiba 2017), with associated studies of impacts on infinite surfaces (Yarin & Weiss 1995; Clanet *et al.* 2004; Eggers *et al.* 2010; Lagubeau *et al.* 2012; Lee *et al.* 2016; Riboux & Gordillo 2016) and other studies focusing on the associated rim destabilization (Roisman & Tropea 2002; Rozhkov *et al.* 2004; Roisman, Horvat & Tropea 2006; Zhang *et al.* 2010; Villermaux & Bossa 2011; Agbaglah, Josserand & Zaleski 2013; Peters, van der Meer & Gordillo 2013). The impact transforms the bulk drop fluid into a sheet (figure 1*a*) radially expanding and then retracting in the air, while being bound by a bulge, a rim, that continuously destabilizes into droplets (figure 1*b*). When the impact Reynolds number $Re = u_0 d_0/\nu$ is high, the impact dynamics on a rod of comparable size, $d_r/d_0 < 1.9$ (Wang & Bourouiba 2017), can be considered as inviscid and is governed by the balance between the fluid inertia and surface tension, namely, the impact Weber number, $We = \rho u_0^2 d_0/\sigma$, where u_0 is the drop impact speed, ρ is the fluid density, ν is its kinematic viscosity and σ is its surface tension.

With especially developed advanced image processing (AIP) algorithms, we (Wang & Bourouiba 2018*b*) showed that the fluid shedding from the rim is continuous and in fact, has a leading-order effect on the sheet's temporal evolution (Wang & Bourouiba 2022). This effect was captured by a non-Galilean Taylor–Culick law, with a peculiar property of time-to-peak invariance: the maximum radius of the sheet is reached at a fixed dimensionless time $T_m = t_m/\tau_{cap}$, independent of impact Weber number and with $T_m = 0.43$, with $\tau_{cap} = \sqrt{\rho \Omega_0/\pi\sigma}$, $\Omega_0 = \pi d_0^3/6$ as the impacting drop volume, and d_0 the drop diameter. This invariance is robust for the dynamics examined over the capillary time scale, τ_{cap}.

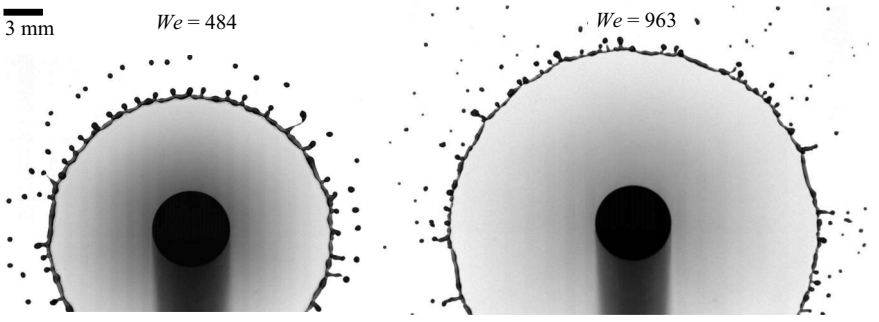

Figure 2. Snapshots of unsteady fragmenting sheets upon drop impact on small rods of comparable size at time $t = 0.2\tau_{cap}$ for two different impact *We*, where $\tau_{cap} = \sqrt{\rho\Omega_0/\pi\sigma}$ is the capillary time and $\Omega_0 = \pi d_0^3/6$ is the impacting drop volume. The impacting drop diameter for both cases is $d_0 = 4.35$ mm. More, though smaller, droplets are generated at higher impact *We*. However, it is unclear if the volume fraction (volume shed over initial drop volume) increases with *We*. This and other related questions of partition of volume, mass, momentum and energy are the focus of this paper.

Figure 2 shows a snapshot of two fragmenting sheets upon impact of drops of the same size, but with different impact *We*. Note that the drops are impacting surfaces of identical rod-to-drop size ratios of $\eta = d_r/d_0 \approx 1.5$, which ensures inviscid sheet dynamics in the air (Wang & Bourouiba 2017). From observation, it would appear as if fragmentation with a higher *We* would lead to more spray, with smaller droplets. However, in light of the subtleties that unsteadiness introduces (Wang & Bourouiba 2018*b*), this and other basic questions are in fact still open. These include:

(i) How does the volume/mass fraction of fluid shed throughout the fragmentation vary with impact *We* or impact energy (§ 5.2)?
(ii) What governs the temporal evolution of the partitioning of volume/mass (§ 5), momentum (§ 6) and energy (§ 7) in the sub-parts of the system – sheet, rim and fluid shed forming the ligaments and droplets? In particular, how does the temporal evolution of volume/mass, momentum and energy change with impact *We* or energy?
(iii) What are the resulting insights gained on dissipative mechanisms in this canonical unsteady fragmentation system (§ 8)?

In this study, we combine experiments and theory to answer the above questions. We derive analytical predictions, without use of fitting parameters, of the temporal evolution of the volume/mass, momentum and energy in each sub-part of the fragmenting system: from sheet, to rim to fluid shed in the form of ligaments and droplets. We validate the predictions against precise measurements for each part. The robustness and regime of validity (*We–Re* map) of the predictions derived are examined with experiments with varying fluid properties and impact conditions (§ 9). We start by reviewing our experimental approach (§ 2) and then the existing theoretical framework of unsteady fragmentation (§§ 3 and 4).

2. Experimental approach and image processing algorithms

2.1. *Experimental approach*

We used two high-speed cameras to simultaneously capture both side and top views of the impact. The frame rates of the top-view and side-view cameras were 20 000 and 8000 frames per second (fps), respectively. An impacting drop was released from a needle at different heights, selecting a range of impacting speeds, u_0. We measured the impact

Fluid	d_0 (mm)	u_0 (m s^{-1})	We	Re ($\times 10^3$)	N_{exp}	Rod diameter
Water	4.35 ± 0.05	1.68 ± 0.01	170 ± 3	7.3 ± 0.1	15	$d_r = 6.3$ mm, $\eta = 1.45$
		2.06 ± 0.01	254 ± 4	9.0 ± 0.2	15	
		2.25 ± 0.01	306 ± 5	9.8 ± 0.2	20	
		2.52 ± 0.01	384 ± 7	10.1 ± 0.2	20	
		2.83 ± 0.01	484 ± 9	12.4 ± 0.3	28	
		3.39 ± 0.01	679 ± 11	14.7 ± 0.2	28	
		4.00 ± 0.01	963 ± 17	17.3 ± 0.3	28	

Table 1. Experimental conditions used, including the impact drop diameter d_0, the impacting speed, u_0, and associated $We = \rho u_0^2 d_0/\sigma$ and $Re = u_0 d_0/\nu$, where $\rho = 1.0 \times 10^3$ kg m^{-3}, $\nu = 1.0 \times 10^{-6}$ m^2 s^{-1} and $\sigma = 72$ mN m^{-1} are the density, kinematic viscosity and surface tension of the water drop, respectively. Here, N_{exp} is the number of experiments per condition.

speed directly from the side high-speed recordings. The drops impacted stainless-steel cylindrical rods of comparable size to that of the impacting drops to ensure formation of a horizontal inviscid expanding sheet in the air (Wang & Bourouiba 2017).

For most of this paper, we present results of a de-ionized water drop with nigrosin dye of concentration 1.2 g l^{-1}, with density $\rho = 1.0 \times 10^3$ kg m^{-3}, surface tension $\sigma = 72 \times 10^{-3}$ N m^{-1} and kinematic viscosity $\nu = 1.0 \times 10^{-6}$ m^2 s^{-1}. Fluids with different properties were used to assess the robustness and regime of validity of the predictions. These included glycerol–water to vary viscosity and dimethyl sulfoxide (DMSO) to vary surface tension. The ranges of the impact Weber and Reynolds numbers were selected to examine the regimes of validity of predictions. These details are discussed in § 9. Each group of experiments was repeated at least 15 times (table 1) with detailed experimental conditions summarized in tables 1 and 2.

2.2. *Advanced image processing (AIP) algorithms*

As described by Wang & Bourouiba (2022), we developed multi-step AIP algorithms to capture all key physical quantities of the sheet, rim, ligaments and secondary droplets listed in figure 1(*b*). These were well captured by our AIP algorithms despite their complex change in morphology and topology over time. For the expanding sheet, we detect the boundary between the sheet and the rim as the contour of the sheet. The radius of the sheet, r_s, can then be captured by measuring the total area, A_s, within the sheet contour and calculating, $r_s = \sqrt{A_s/\pi}$ (figure 3*a*). The sheet spatio-temporal thickness profile, $h(r, t)$, was derived and validated via light absorption, and the sheet velocity profile, $u(r, t)$, was derived and validated by particle tracking velocimetry (Wang & Bourouiba 2017). With these quantities determined, the fluid volume, momentum and energy in the sheet are quantified experimentally.

We note that, beside water, nigrosin can also be dissolved in other liquids. Table 2 includes some of these: glycerol–water mixture and DMSO. Nigrosin dye at concentration 1.2 g l^{-1} was added to these liquids. Figure 3 shows that the absorption of the different nigrosin-dyed liquids follow the Beer–Lambert law of absorption well, with

$$\log(I/I_0) = ch \Longrightarrow h = -\frac{1}{c}\log(I/I_0), \tag{2.1}$$

where I_0 is the background light intensity and I is the intensity of the light transmitted through the dyed liquid of a given thickness h. Here, c is the liquid absorptivity.

https://doi.org/10.1017/jfm.2021.625 Published online by Cambridge University Press

Fluid	ρ (g cm^{-3})	σ (mN m^{-1})	μ (mPa s)	d_0 (mm)	u_0 (m s^{-1})	*We*	*Re* ($\times 10^3$)	N_{exp}	Rod diameter
DMSO	1.10	42 ± 2	2.0	3.76	1.46	210	3.02	10	$d_r = 6$ mm, $\eta = 1.59$
				3.79	1.76	307	3.67	10	
				3.80	2.44	593	5.10	20	
				3.75	2.97	872	6.23	30	
Glycerol (50 %)	1.13	69 ± 2	5.2	4.08	3.24	677	2.95	20	$d_r = 6.3$ mm, $\eta = 1.57$
Glycerol (70 %)	1.18	67 ± 2	20	4.02	3.49	862	0.91	15	

Table 2. Properties of fluids used in this study, with corresponding initial conditions and associated Weber, *We*, and Reynolds, *Re*, numbers. Glycerol–water mixtures were used to vary viscosity, with the percentage indicating mass fraction. DMSO was used to vary surface tension. The impact target diameters used were chosen to ensure drop-to-target size ratios, η, between 1.4 and 1.9, which ensures horizontal sheet expansion and negligible surface stresses.

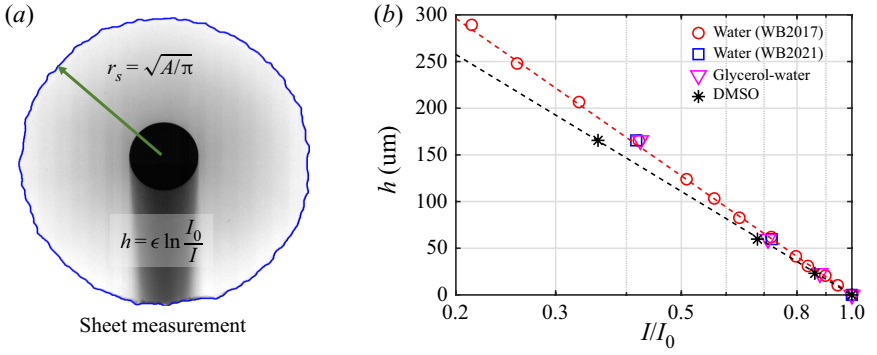

Figure 3. (*a*) Sheet contour detection and the light absorption method using nigrosin-dyed liquid to measure the sheet thickness. (*b*) Calibration curves mapping liquid sheet thickness to transmitted light intensity ratio I/I_0 for different fluids laden with nigrosin dye of concentration 1.2 g l^{-1}. Here, I is the intensity of the light transmitted through the fluid sheet, while I_0 is the background light intensity. WB2017 indicates data from Wang & Bourouiba (2017), while WB2021 indicates data of the present study.

The measured fluid absorptivity of dyed liquid water $c = \frac{1}{185}\ \mu\text{m}^{-1}$ matches that measured by Wang & Bourouiba (2017), which further supports the robustness of this light absorption methodology for sheet thickness measurements. Glycerol–water mixtures of the same nigrosin concentration also have similar fluid absorptivity c to that of water, while DMSO with the same nigrosin concentration has a slightly larger fluid absorptivity $c = \frac{1}{160}\ \mu\text{m}^{-1}$.

For the rim and ligaments, we first detect the inner and outer contours of the rim–ligament connection. By setting the extruded parts to be the ligaments, our AIP algorithms can systematically and precisely separate the ligaments from the rim (figure 4*a*). Upon separation, the thickness of the rim, b, is measured locally at each angular position and averaged along the rim. The length of each ligament, ℓ, is measured as the curvilinear distance from its root to its tip. The width of each ligament, w, is measured locally at each cross-section and averaged along the centreline of the ligament (inset of figure 4*a*). The volumes of the rim and ligaments are measured by assuming axisymmetric cross-sections. The tips of the ligaments detected at each frame are linked together by our ligament-tracking algorithms (Wang & Bourouiba 2018*b*) enabling to track the evolution of each ligament throughout the sheet evolution – expansion and retraction – and measure their tip velocity. The rim's velocity is measured by taking the derivative of the sheet radius. With the geometry and velocity of the rim and ligaments determined, the fluid volume, momentum and energy in the rim and the ligaments are quantified experimentally.

For the secondary droplets, their sizes and positions are detected at each frame (figure 4*b*) and linked into trajectories (figure 4*c*) by our droplet-tracking algorithms (Wang *et al.* 2018). The initial time of formation of each trajectory is the time at which the droplet is shed. The ejection speed of a droplet is its speed at time of shedding. With the size, speed and shedding time of each droplet, the cumulative volume shed, Ω_d, as well as the associated momentum and energy of the droplets shed throughout the fragmentation, are quantified experimentally. Finally, note that the accuracy of the AIP algorithms was established by Wang & Bourouiba (2022), who showed that the fluid volume in all sub-parts of the fragmentation system sum up, at all times, to the initial volume of the impacting drop Ω_0. The AIP algorithms, used here as well, capture both cumulative and instantaneous volume conservation.

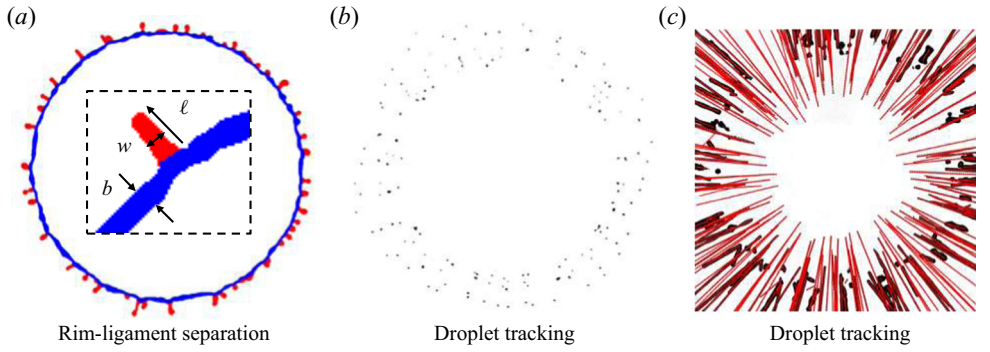

Figure 4. Key steps of our AIP algorithms, including (*a*) contour detection of the rim and ligaments and their separation; and secondary droplet (*b*) detection and (*c*) tracking.

3. Review of unsteady sheet evolution

3.1. *Dynamics of rim destabilization and thickness*

A number of prior studies have focused on rim destabilization via linear stability analysis (Roisman & Tropea 2002; Zhang *et al.* 2010; Villermaux & Bossa 2011; Peters *et al.* 2013). It was shown that the rim initially destabilizes into small corrugations due to a local interplay of interfacial (Rayleigh–Plateau) and inertial (Rayleigh–Taylor) instabilities accounting for the continuous deceleration of the rim (Krechetnikov & Homsy 2009; Wang *et al.* 2018). However, upon fragmentation, the fluid shed from the rim is in the form of ligaments (rather than small-amplitude corrugations). Here, nonlinear effects dominate (Roisman, Berberovi & Tropea 2009; Agbaglah *et al.* 2013; Wang *et al.* 2018) and linear instability predictions consequently no longer capture the observations. Wang *et al.* (2018) showed that, in fact, the non-Galilean frame of the rim with time-varying deceleration imposes an instantaneous self-adjustment of the rim thickness, b, which remains equal to the local and instantaneous capillary length as defined by the instantaneous sheet acceleration, $\ddot{r}_s$. This can be expressed as

$$Bo = \frac{\rho b^2(-\ddot{r}_s)}{\sigma} = 1 \Longrightarrow b = \sqrt{\frac{\sigma}{\rho(-\ddot{r}_s)}}, \tag{3.1}$$

where Bo is a local and instantaneous Bond number. Such self-adjustment of the rim thickness governed by the $Bo = 1$ criterion indirectly determines the volume of fluid continuously shed from the rim during unsteady fragmentation. Here, we note that fluid shedding from the rim of a stationary sheet, such as a Savart sheet upon impact of a continuous liquid jet (Savart 1833; Clanet & Villermaux 2002), is clearly not governed by the (3.1) constraint. Gordillo, Lhuissier & Villermaux (2014) reported another fluid shedding mechanism for such stationary sheets, determined by the Taylor–Culick speed recession and cusps forming along the sheet, leading to a shedding velocity $v_\ell \approx u_0/5$, where u_0 is the impact velocity of the liquid jet. Figures 1(*b*) and 2 show that the contour of the liquid sheet in unsteady fragmentation is nearly circular in contrast to the cusp-containing shape of stationary sheets (Gordillo *et al.* 2014). In the interest of concision, details on how rim deceleration induces fluid shedding during cusp-free unsteady sheet fragmentation discussed by Wang & Bourouiba (2021) are not repeated here.

3.2. *Non-Galilean Taylor–Culick's law for the sheet radius, $r_s(r, t)$*

Wang & Bourouiba (2018*b*) showed that droplets are shed continuously during the sheet evolution – expansion and retraction – with most shedding, in fact, occurring prior to the sheet's maximum extension. Using our AIP algorithms, we (Wang & Bourouiba 2022) showed that the fluid shed from the rim has a leading-order effect on the sheet evolution, namely, the unsteady sheet evolution is coupled with the fluid shedding and resulting droplet fragmentation during the entire process. Wang & Bourouiba (2022) derived a modified theory of unsteady sheet evolution which incorporated the coupled inertial and fluid shedding effects, leading to the following governing equation for the sheet radius, $r_s(r, t)$:

$$\left.\begin{array}{c} (\dot{ar_s}) = q_{in} - q_{out}, \\ (\rho a r_s)\ddot{r_s} - \rho q_{in}(u(r_s, t) - \dot{r_s}) + \rho q_{out} v_\ell + 2\sigma r_s = 0, \\ \text{with } a = \pi b^2/4 \text{ and } q_{in}(t) = h(r_s, t) r_s(t)(u(r_s, t) - \dot{r_s}), \end{array}\right\} \tag{3.2}$$

where $\langle\cdot\rangle$ is the derivative with respect to time, the sheet velocity profile is $u(r_s, t) = r_s/t$ (Wang & Bourouiba 2017), a is the cross-sectional area of the rim, q_{in} is the volume rate – volume per unit of time and unit radian – entering the rim, q_{out} is the volume rate of fluid shed from the rim per unit of time and radian, and v_ℓ is the speed of fluid leaving from the rim into the ligaments in the reference frame of the rim. Based on the self-adjustment of the rim thickness governed by the $Bo = 1$ criterion, the volume rate q_{out} is directly determined by mass conservation in (3.2). In addition, Wang & Bourouiba (2022) showed that the fluid outward speed v_ℓ is determined by the local dynamics of the ligament–rim junction. With $Bo = 1$ and v_ℓ determined, the governing equation of unsteady sheet radius is shown to reduce to

$$-\rho h(r_s, t)\left(\frac{r_s}{t} - \dot{r_s}\right)^2 + \left(2 - \frac{\pi}{7}\right)\sigma = 0, \tag{3.3}$$

referred to as a non-Galilean Taylor–Culick law, due to its similarity with the classical Taylor–Culick relation, but with an additional term $-\pi\sigma/7$ shown to incorporate the unsteadiness, inertial and shedding effects.

By choosing the characteristic length scale to be the impacting drop diameter, d_0, and the characteristic time scale to be the capillary time, $\tau_{cap} = \sqrt{\rho\Omega_0/\pi\sigma} = \sqrt{\rho d_0^3/6\sigma}$, the non-dimensional time T, sheet radius R_s and thickness H are

$$T = \frac{t}{\tau_{cap}}, \quad R_s = \frac{r_s}{d_0} \quad \text{and} \quad H = \frac{h}{d_0}. \tag{3.4a–c}$$

Thus, the non-dimensional form of (3.3) reads

$$-6H(R_s, T)\left(\frac{R_s}{T} - \dot{R_s}\right)^2 + \left(2 - \frac{\pi}{7}\right) = 0, \tag{3.5}$$

where $H(R_s, T)$, the sheet thickness at the rim, is

$$H(R_s, T) = \frac{T\sqrt{6We}}{6a_3 R_s(T)^3 + a_2 R_s(T)^2 T\sqrt{6We} + a_1 R_s(T) T^2 We}, \tag{3.6}$$

where a_1, a_2 and a_3 are the constant coefficients of the sheet thickness profile that was derived and validated by Wang & Bourouiba (2017).

3.3. *Time-to-peak invariance*

Armed with (3.5), a nonlinear equation, Wang & Bourouiba (2022) revealed and validated that the unsteady sheet dynamics has a peculiar property of invariance of time-to-peak: the evolution of the sheet radius, $R_s(T)$, over dimensionless time T non-dimensionalized by the capillary time scale τ_{cap}, is independent of impact We or energy. Namely, the sheet radius, $R_s(T)$, is expressed as

$$R_s(T) = \sqrt{We}\, Y_0(T), \tag{3.7}$$

reaches its maximum value at a time $T_m = 0.43$ independent of the impact We or energy, with an approximate analytical expression of $Y_0(T)$ derived to be

$$\left.\begin{aligned} Y_0(T) &= 0.15(T - T_m)^3 - 0.4(T - T_m)^2 + \mathcal{R}_m, \\ \text{with } T_m &= 0.43 \text{ and } \mathcal{R}_m = R_m/\sqrt{We} = 0.12. \end{aligned}\right\} \tag{3.8}$$

In the remainder of this paper, we show that such a property of time invariance has important implications for the temporal evolution of volume/mass, momentum and energy of the fluid system and their partition in its sub-parts: from sheet, to rim to fluid shed.

4. Dependence of sheet and rim thickness on *We*

Using the sheet radius, $r_s(t)$, and non-Galilean Taylor–Culick's law (3.3), the volume of fluid shed per unit of time and radian – volume rate – by the rim is directly derived from mass conservation at the rim (3.2) to read as

$$q_{out} = \underbrace{q_{in}}_{\text{rate of volume entering the rim}} - \underbrace{(a\dot{r_s})}_{\text{rate of change of the rim's volume}}. \tag{4.1}$$

Using (3.2), q_{out} can be expanded to read

$$q_{out} = h(r_s, t) r_s \left(\frac{r_s}{t} - \dot{r_s}\right) - \frac{\mathrm{d}}{\mathrm{d}t}\left(\frac{\pi}{4} b^2 r_s\right). \tag{4.2}$$

Thus, the two fundamental quantities required to determine the volume transfer between the sheet, the rim and the fluid shed from the rim are the sheet thickness at the rim, $h(r_s, t)$, and the rim thickness, $b(t)$. Using (3.6) and (3.7), $H(R_s, T) = h(r_s, t)/d_0$ reads

$$H(R_s, T) = \frac{1}{We}\Phi(T) \quad \text{where } \Phi(T) = \frac{\sqrt{6}T}{6a_3 Y_0(T)^3 + \sqrt{6}a_2 Y_0(T)^2 T + a_1 Y_0(T) T^2}, \tag{4.3}$$

where a_1, a_2 and a_3 are the coefficients of the sheet thickness profile derived by (Wang & Bourouiba 2017) and $Y_0(T)$ is the universal function of sheet radius, which are all known and independent of We. Equation (4.3) gives that the sheet thickness at the rim scales as We^{-1}, so that $H(R_s, T)We$ follows a time evolution function $\Phi(T)$, independent of We. Figure 5(*b*) shows the measured time evolution of $H(R_s, T)$ for different We, normalized by We^{-1}, with all curves collapsing on a single curve. The solid line shows that the prediction (4.3) captures the data well. We quantify the agreement between data and theory, showing the ratio of the measured to predicted quantity, for each We, in the figure insets (e.g. figure 5*b*). Here, the ratio remains close to one for the entire dynamics, which confirms the good agreement between prediction and measurement. In addition,

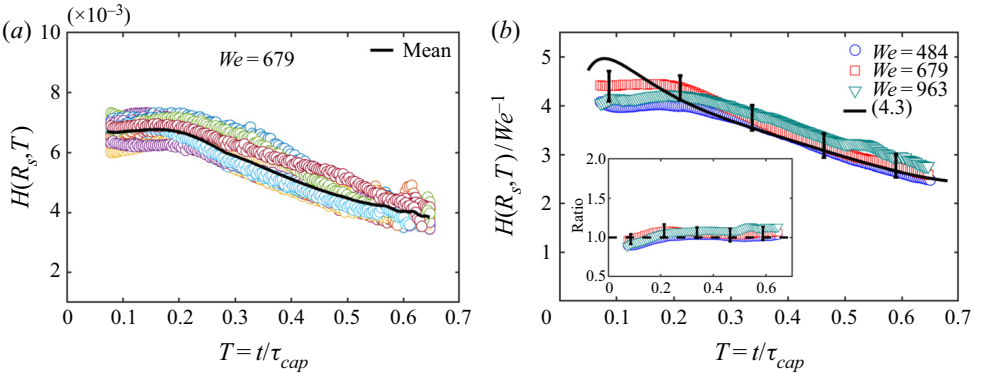

Figure 5. (*a*) Measured time evolution of the sheet thickness at the rim, $H(R_s, T)$, non-dimensionalized by the impacting drop diameter, d_0, from 28 repeated experiments (different colours) for $We = 679$. The solid line shows the mean of 28 experiments. (*b*) Measured time evolution of sheet thickness at the rim, $H(R_s, T)$, for different impact We. Normalized by We^{-1} all data collapse on a single curve. The solid line shows that the prediction (4.3) of $H(R_s, T)$, captures the data well. Error bars indicate the standard deviation across all repeated experiments for each group. The inset shows that the ratio of the measured data with the prediction remains equal to one during the entire fragmentation, which indicates good agreement between prediction and measurements.

figure 5(*a*) shows the measured time evolution of $H(R_s, T)$ from all 28 experiments (see table 1) for $We = 679$, all of which follow a similar trend, which indicates a reproducibility of the experiments. We note that each curve in figure 5(*b*) represents the mean of all experiments for a given experimental condition. The confidence interval (error bar) in figure 5(*b*) indicates the standard deviation across all those experiments. Unless specified otherwise, the same convention regarding computation and rendering of error bars in the figures is used throughout the remainder of the paper.

The rim, $b(t)$, governed by the $Bo = 1$ criterion (§ 3.1), maintains its thickness equal to the instantaneous capillary length associated with the instantaneous rim acceleration. Figure 6(*a*) shows that the rim acceleration can be well captured by the full prediction of the non-Galilean Taylor–Culick law (3.5). Similar to the sheet radius R_s (3.7), the rim acceleration $\ddot{R}_s$ also scales as $\sqrt{We}$. Using (3.1) and (3.7), the non-dimensional rim thickness, $B(T) = b(T)/d_0$, reads

$$B(T) = (-6\ddot{R}_s(T))^{-1/2} = \frac{1}{We^{1/4}}\Psi(T) \quad \text{with } \Psi(T) = [-6\ddot{Y}_0(T)]^{-1/2}, \tag{4.4}$$

which scales as $We^{-1/4}$. The measured time evolution of the dimensionless rim thickness, B, for different We, normalized by $We^{-1/4}$, collapse on a single curve (figure 6*b*). The solid line shows that the prediction (4.4) of the rim thickness $B(T)$ captures the data very well. Note that the rim thickness scaling as $B \sim We^{1/4}$ from the $Bo = 1$ criterion coupled with the shedding assumption happen to coincidentally emerge as scaling for the rim's thickness when also assuming no shedding from the rim (Villermaux & Bossa 2011). Thus, the validity of this scaling does not inform about shedding. The cumulative volume of fluid shed from the rim was however shown to remain of the same order of magnitude as the rim's volume throughout the sheet dynamics (see Wang & Bourouiba (2022) and figure 10*b*).

We have now recalled the derived equations governing the sheet evolution: that of the sheet radius, $R_s(T)$, the sheet thickness at the rim, $H(R_s, T)$, and the rim thickness, $B(T)$, and we have shown how each quantity scales with We. We now leverage these results

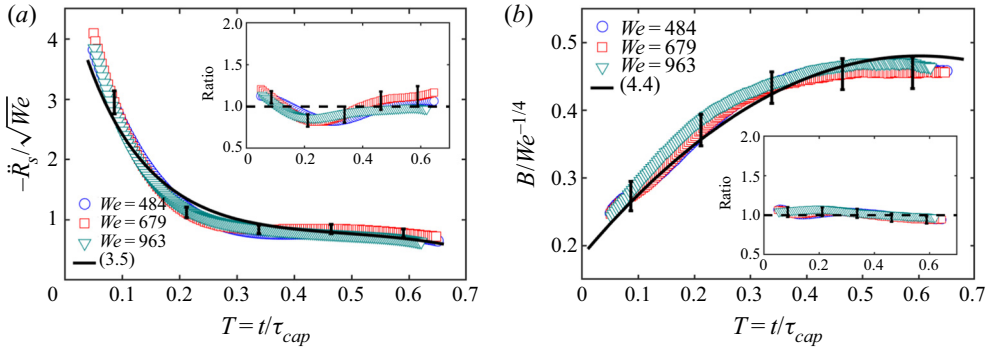

Figure 6. (*a*) Measured time evolution of the rim deceleration, $-\ddot{R}_s$, non-dimensionalized by the acceleration scale, d_0/τ_{cap}^2. When normalized by $\sqrt{We}$, all data collapse on a single curve. The solid line shows that the full prediction of $\ddot{R}_s$ from (3.5) captures the data well. (*b*) Measured time evolution of the rim thickness, B, non-dimensionalized by d_0. When normalized by $We^{-1/4}$, all data collapse on a single curve. The solid line shows that the prediction (4.4) captures the data well. Error bars in both panels (*a*) and (*b*) indicate the standard deviation across all repeated experiments in each group of experimental conditions. Both insets show the ratio of the measurement to prediction of the relevant properties. These remain close to one, which indicates a good agreement between prediction and data.

to determine and verify the temporal evolution of the volume/mass partitioning in each sub-part of the fluid system: the sheet, the rim and the fluid shed from the rim, which forms the ligaments and droplets. Hereafter, unless noted otherwise, the sheet includes the sheet in the air, as well as the fluid on the rod. The fluid shed from the rim includes both the ligaments and ejected secondary droplets.

5. Volume/mass partitioning in the sub-parts of the system

5.1. *Volume/mass fraction in the rim*

Taking the rim to be cylindrical, its dimensional volume, Ω_{rim}, is

$$\Omega_{rim}(t) = 2\pi r_s(t)\frac{\pi}{4}b^2(t), \tag{5.1}$$

which in dimensionless form is

$$\mathcal{V}_{rim}(T) = \frac{\Omega_{rim}/2\pi}{d_0^3} = \frac{\pi}{4}R_s(T)B(T)^2 = \frac{\pi}{4}Y_0(T)\Psi^2(T), \tag{5.2}$$

where the expressions of sheet radius (3.7) and rim thickness (4.4) were used. In addition, the impacting drop volume $\Omega_0 = \pi d_0^3/6$ is non-dimensionalized as

$$\mathcal{V}_0 = \frac{\Omega_0/2\pi}{d_0^3} = \frac{1}{12}. \tag{5.3}$$

Thus, the volume fraction in the rim becomes

$$\frac{\mathcal{V}_{rim}(T)}{\mathcal{V}_0} = 3\pi Y_0(T)\Psi^2(T), \tag{5.4}$$

so the evolution of the fluid volume fraction in the rim governed by the $Bo = 1$ criterion is clearly independent of We. This is indeed verified by our data (figure 7*a*).

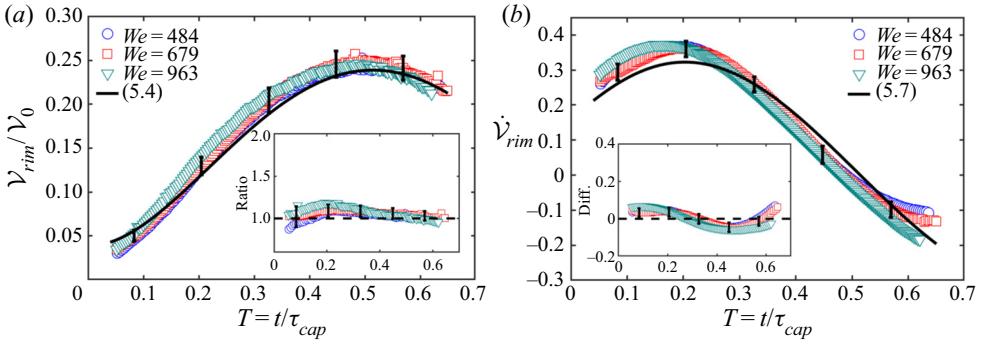

Figure 7. (*a*) Measured time evolution of the volume fraction in the rim, $\mathcal{V}_{rim}(T)/\mathcal{V}_0$, for different impact *We*. All data collapse on a single curve, showing independence from *We*. The solid line shows its prediction (5.4). The inset shows the ratio of measured data and prediction, which remains close to one, indicating good agreement between predictions and data. (*b*) Measured time evolution of the rate of change of the rim volume $\dot{\mathcal{V}}_{rim}$ for different *We*, which also collapse on a single curve and is well captured by our prediction (5.7). The inset shows the difference between measurement and prediction, which is close to zero, indicating good agreement between prediction and data. Error bars indicate the standard deviation across all repeated experiments in each group.

5.2. *Volume/mass fraction in the fluid shed from the rim: ligaments and droplets*

In terms of fluid shed from the rim, in the form of ligaments and droplets, the key quantity is the fluid volume shed from the rim per unit of time, Q_{out}, which from the rim's mass conservation, (3.2), is

$$Q_{out}(T) = Q_{in}(T) - \dot{\mathcal{V}}_{rim}(T). \tag{5.5}$$

To derive an explicit expression, we next determine the volume entering the rim per unit of time and radian, $Q_{in}(T)$, and the rate of change of the rim's volume, $\dot{\mathcal{V}}_{rim}(T)$, separately.

5.2.1. *Rate of change of volume fraction in the rim: $\dot{\mathcal{V}}_{rim}$*

From (5.1), the rate of change of the rim volume over time is

$$\dot{\Omega}_{rim}(t) = \frac{\mathrm{d}}{\mathrm{d}t}\left[2\pi r_s(t)\left(\frac{\pi}{4}b^2(t)\right)\right], \tag{5.6}$$

and in non-dimensional form is

$$\dot{\mathcal{V}}_{rim}(T) = \frac{\dot{\Omega}_{rim}/2\pi}{d_0^3/\tau_{cap}} = \frac{\mathrm{d}}{\mathrm{d}T}\left[\frac{\pi}{4}Y_0(T)\Psi^2(T)\right], \tag{5.7}$$

which is also independent of *We* as verified by our data, that is well captured by our prediction (5.7) (figure 7*b*).

5.2.2. *Volume fraction entering the rim*

We start with the rate of volume injection into the rim from the sheet per radian, $q_{in}(t)$, which was expressed in (3.2). In non-dimensional form, it reads

$$Q_{in}(T) = \frac{q_{in}}{d_0^3/\tau_{cap}} = H(R_s, T)R_s(T)\left(\frac{R_s(T)}{T} - \dot{R}_s(T)\right). \tag{5.8}$$

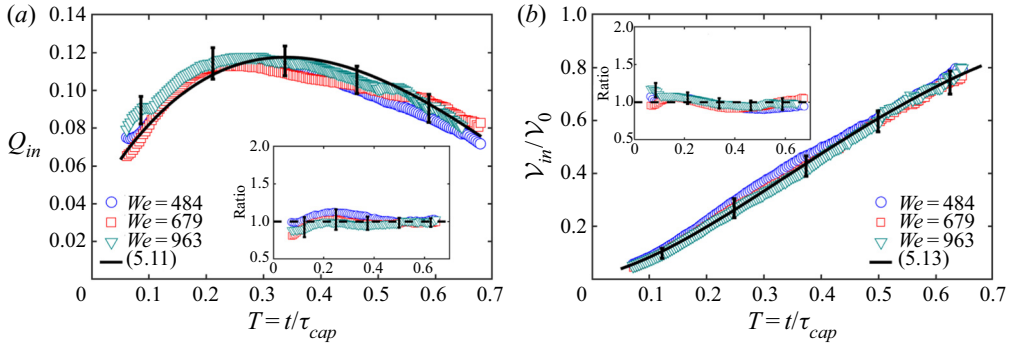

Figure 8. (*a*) Measured time evolution of the rate of volume entering the rim per unit radian, Q_{in}, for different impact *We*, which all collapse on a single curve, indicating independence from *We*. The solid line shows that our prediction (5.11) captures the data well. (*b*) Measured time evolution of the cumulative volume fraction entering the rim, $\mathcal{V}_{in} = \Omega_{in}(T)/\Omega_0$, is also independent of *We* and is well captured by our prediction (5.13) (solid line). Both insets show that the ratios of measurement to prediction remain close to one, which indicates good agreement between prediction and data. Error bars indicate the standard deviation across all repeated experiments in each group.

Using the sheet radius expression (3.7) and the sheet thickness at the rim, (4.3) reads

$$Q_{in}(T) = \frac{1}{We}\Phi(T)WeY_0(T)\left(\frac{Y_0(T)}{T} - \dot{Y}_0(T)\right) = \Phi(T)Y_0(T)\left(\frac{Y_0(T)}{T} - \dot{Y}_0(T)\right), \tag{5.9}$$

which is interestingly also independent of impact *We* . This expression, (5.9), is an explicit form of the volume entering the rim per unit of time and radian, $Q_{in}(T)$. It can be further simplified using (3.5) to

$$\frac{R_s(T)}{T} - \dot{R}_s(T) = \frac{\alpha}{\sqrt{H(R_s, T)}} \quad \text{with } \alpha = \sqrt{\frac{2-\pi/7}{6}}. \tag{5.10}$$

Substituting (5.10) into (5.9) gives

$$Q_{in}(T) = \alpha\sqrt{H(R_s, T)}R_s(T) = \alpha\sqrt{\Phi(T)}Y_0(T). \tag{5.11}$$

The solid line in figure 8(*a*) shows that our prediction (5.11) captures the data well.

The non-dimensionalized cumulative volume entering the rim from the sheet is thus

$$\mathcal{V}_{in}(T) = \int_0^T Q_{in}(T')\,\mathrm{d}T' = \int_0^T \alpha\sqrt{\Phi(T')}Y_0(T')\,\mathrm{d}T'. \tag{5.12}$$

Normalized by the impacting drop volume $\mathcal{V}_0$, the fraction of cumulative volume entering the rim is

$$\frac{\mathcal{V}_{in}(T)}{\mathcal{V}_0} = 12\int_0^T \alpha\sqrt{\Phi(T')}Y_0(T')\,\mathrm{d}T', \tag{5.13}$$

which is also independent of the impact *We* as verified by the data in figure 8(*b*). Thus, at each instant of dimensionless time, the cumulative volume fraction emanating from the sheet into the rim, with respect to the impacting drop volume is, in fact, independent of *We*.

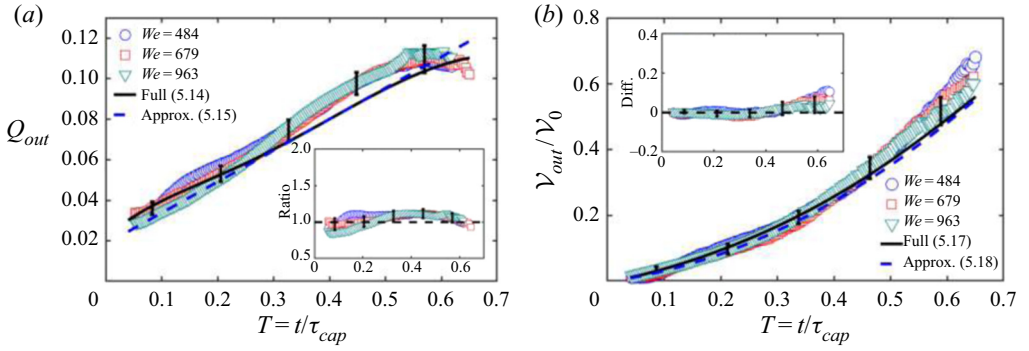

Figure 9. (*a*) Measured time evolution of the volume rate shed per radian from the sheet into the rim for different impact *We*. All data collapse on a single curve, which indicates independence from *We*. The solid and dashed lines show the full prediction (5.14) and the approximate explicit expression (5.15) of Q_{out}, respectively. The inset shows that the ratio of the measured data and prediction remains close to one, which indicates good agreement between prediction and data. (*b*) Measured time evolution of the cumulative volume fraction $\mathcal{V}_{out}(T)/\mathcal{V}_0$ shed from the rim into ligaments–droplets, for different *We*, is also independent of *We* and is well captured by its full prediction (5.17), as well as the approximate expression (5.18). The inset shows the difference between measured data and prediction, which remains close to zero, indicating good agreement between prediction and data. Error bars indicate the standard deviation across all repeated experiments in each group.

Having determined the volume entering the rim per unit of time and radian, Q_{in}, with (5.11), and the rate of change of rim volume, $\dot{\mathcal{V}}_{rim}$, with (5.7),

$$Q_{out}(T) = \alpha\sqrt{\Phi(T)}Y_0(T) - \frac{\pi}{4}\frac{\mathrm{d}}{\mathrm{d}T}[Y_0(T)\Psi^2(T)], \tag{5.14}$$

where α is the constant given in (5.10). Since both Q_{in} and $\dot{\mathcal{V}}_{rim}$ are independent of *We*, the volume shed per unit of time and radian from the rim, Q_{out}, is also independent of *We*. This is verified by our data in figure 9*a*, which are very well captured by our prediction (5.14) (solid line). In addition, the volume rate shed, Q_{out}, appears to monotonically increase with time at a nearly constant rate. Taking this functional form (see § A.4) would read

$$Q_{out} = p_0 + p_1(T - T_m), \tag{5.15}$$

where $T_m = 0.43$ is the time of maximum sheet radius (Wang & Bourouiba 2022), $p_0 = 0.09$ is the volume shed per unit of time and radian at T_m, and $p_1 = 0.15$ is the approximate increase rate of the volume rate shed throughout the sheet evolution. Note that p_1 and p_2 are not fitted but both are derived theoretically in § A.4.

From the prediction of volume rate shed, Q_{out}, we can directly determine the time evolution of the non-dimensionalized volume in the ligaments and droplets shed from the rim,

$$\mathcal{V}_{out} = \int_0^T Q_{out}(T')\,\mathrm{d}T' = \int_0^T \alpha\sqrt{\Phi(T')}Y_0(T')\,\mathrm{d}T' - \frac{\pi}{4}Y_0(T)\Psi^2(T). \tag{5.16}$$

Normalized by the impacting drop volume $\mathcal{V}_0$, the fraction of volume shed from the rim gives

$$\frac{\mathcal{V}_{out}}{\mathcal{V}_0} = 12\int_0^T \alpha\sqrt{\Phi(T')}Y_0(T')\,\mathrm{d}T' - 3\pi Y_0(T)\Psi^2(T), \tag{5.17}$$

which can be shown (see § A.4) to reduce to

$$\frac{\mathcal{V}_{out}}{\mathcal{V}_0} = 12p_0(T - T_m) + 6p_1(T - T_m)^2. \tag{5.18}$$

Figure 9(*b*) shows that both the full prediction (5.17) of the time evolution of measured cumulative volume shed from the rim normalized by Ω_0 and its approximate explicit form (5.18) capture the data very well for all *We*. Interestingly, the resulting cumulative volume fraction shed amounts to 70 % of the original drop volume, regardless of impact energy.

Recalling our first question in § 1 : How does the volume fraction of fluid shed throughout the fragmentation vary with impact *We* or impact energy? We have shown that

(i) the temporal evolution of the dimensionless rate of volume shed from the rim, $Q_{out}(T)$, to form ligaments and droplets, is approximately linearly increasing over time; and
(ii) that the volume fraction of fluid shed, Q_{out}, from the rim at each instant and cumulatively, $\mathcal{V}_{out}$, are both also independent of the impact *We* or impact energy.

In sum, the fractions of impacting drop volume shed at any given time and cumulatively, are, in fact, both independent of the impact *We* or energy. A resulting 70 % of the impacting drop volume/mass is shed, regardless of impact energy, by the dimensionless time $T = 0.7$, up to which point the sheet conserves its integrity free of inner punctures. Beyond that time, the sheet can punctures around the solid surface of the rod, depending on its surface properties, and particularly for higher impact *We*, since the sheet thickness monotonically decreases with the impact *We* (Wang & Bourouiba 2017). For example, the measured sheet thickness around the edge of the rod at $T = 0.7$ for $We = 963$ is less than 20 μm. This rupture of sheets around the edge of the solid surface from which they emanate along with collision of rims were reported and studied in prior work (Villermaux & Bossa 2011; Lejeune, Gilet & Bourouiba 2018; Néel, Lhuissier & Villermaux 2020).

5.3. *Volume/mass fraction in the sheet and summary of volume/mass partitioning*

With the fraction of cumulative volume having entered the rim $\mathcal{V}_{in}(T)$ at time T determined in (5.13), the fraction of impacting drop volume remaining in the sheet at that time T is

$$\frac{\mathcal{V}_s(T)}{\mathcal{V}_0} = 1 - \frac{\mathcal{V}_{in}(T)}{\mathcal{V}_0} = 1 - 12\int_0^T \alpha\sqrt{\Phi(T')}Y_0(T')\,\mathrm{d}T', \tag{5.19}$$

which is clearly independent of *We* (figure 10*a*). In sum, we have discovered that the volume fractions in the sheet, $\mathcal{V}_s$, in the rim, $\mathcal{V}_{rim}$, and in the fluid shed from the rim in the form of ligaments and droplets, $\mathcal{V}_{out}$, are in fact all independent of impact *We*. This is verified by the summary of all measured volume fractions in the fluid system (figure 10*b*). When examining the effect of volume shed from the rim on the sheet evolution, the cumulative volume shed should be compared with the instantaneous rim volume rather than the total impacting drop volume. This is because the dynamics of the rim is derived from control volume theory, with the rim being the control volume. Hence, although the cumulative fluid shedding amounts to approximately 20–30 % (figure 10*b*) of the impacting drop volume, the cumulative volume shed from the rim is in fact of the same order of magnitude as that of the rim at any given time during most of the sheet expansion (figure 10*b*). We therefore cannot neglect shedding. Doing so would amount to an overestimation of the rim's volume by 100 %.

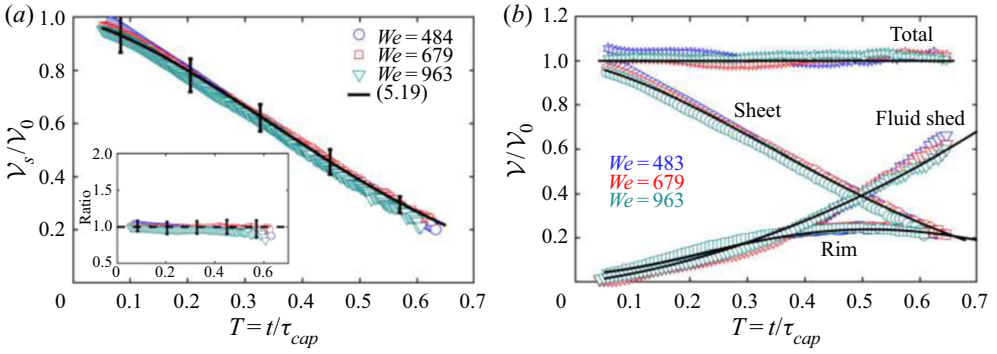

Figure 10. (*a*) Measured time evolution of the volume fraction in the sheet, $\mathcal{V}_s = \Omega_s(T)/\Omega_0$, including the sheet in the air and on the rod, for different *We*. All data collapse on a single curve, which indicates independence of the the mass fraction in the sheet (air and rod) from *We*. The solid line shows that the prediction (5.19) matches the data well. The inset shows that the ratio of measured data to prediction is close to one, which indicates a good agreement between prediction and data. (*b*) Measured time evolution of the volume fractions in different sub-parts of the system. For each sub-part, the data for different *We* collapse on a single curve, which indicates independence from *We*. The solid lines show the predictions of the volume fractions in each sub-part are in good agreement with the data and recovering the total impacting drop volume, Ω_0. This confirms that the cumulative volume shed, at a given time, from the rim remains of the same order of magnitude as the instantaneous rim volume.

Finally, given incompressibility, the mass fractions in each part of the fluid system – sheet, rim and ligaments–drops shed – are immediately deduced from the volume fractions derived above, by simply multiplying volumes by the fluid density ρ. The mass fractions in each sub-part are thus also all independent of impact *We*.

In the next sections, we turn to the momentum and energy partitioning in each sub-part of the system.

6. Momentum partitioning in each sub-part of the fluid system

6.1. *Fraction of momentum in the rim*

We now examine the evolution of the momentum in each sub-part of the system. Starting with the rim, its momentum is

$$p_{rim}(t) = \rho \Omega_{rim}(t) \dot{r}_s(t), \tag{6.1}$$

and in dimensionless form reads

$$P_{rim}(T) = \frac{p_{rim}/2\pi}{\rho d_0^4/\tau_{cap}} = \frac{1}{12}\mathcal{V}_{rim}(T)\dot{R}_s(T) = \sqrt{We}\frac{\pi}{4}Y_0(T)\Psi^2(T)\dot{Y}_0(T), \tag{6.2}$$

where (5.4) and (3.7) were used. Equation (6.2) explicitly depends on $\sqrt{We}$. The non-dimensional impacting drop momentum, $p_0 = \Omega_0 u_0$ is

$$P_0 = \frac{\rho \Omega_0 u_0/2\pi}{\rho d_0^4/\tau_{cap}} = \frac{1}{12\sqrt{6}}\sqrt{We}. \tag{6.3}$$

Thus, the momentum fraction in the rim is

$$\frac{P_{rim}(T)}{P_0} = 3\sqrt{6}\pi Y_0(T)\Psi^2(T)\dot{Y}_0(T), \tag{6.4}$$

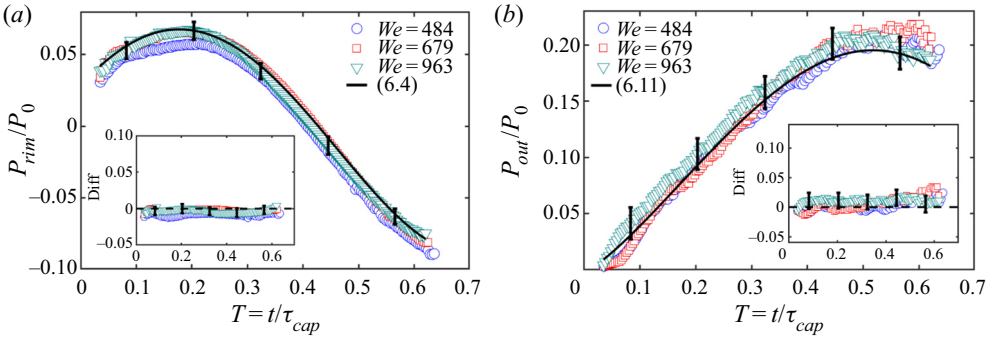

Figure 11. Measured time evolution of (*a*) the fraction of momentum in the rim and (*b*) the cumulative momentum fraction shed from the rim for different impact *We*. All data collapse on a single curve, which indicates that both the fraction of momentum in the rim and the fraction of momentum shed from the rim are independent of *We*. The solid lines show that our predictions (6.4) and (6.11) capture the data very well. Both insets show that the difference between measured data and prediction remains zero, which indicates good agreement between prediction and data. Error bars indicate the standard deviation across all repeated experiments in each group.

which is independent of *We* as verified by our data (figure 11*a*). The solid line in figure 11(*a*) shows that our prediction of fraction of momentum in the rim, (6.4), captures the data very well and is independent of *We*.

6.2. *Fraction of momentum in the fluid shed: ligaments and droplets*

Turning to the momentum in the ligaments–droplets sub-parts of the system, consider the rate of volume shedding from the rim, q_{out}, per radian. The associated rate of momentum shedding from the rim into the ligaments–droplets, $\dot{p}_{out}$, per radian, is then

$$\dot{p}_{out}(t) = \rho q_{out}(t)[\dot{r_s}(t) + v_\ell(t)], \tag{6.5}$$

where $v_\ell(t)$ is the fluid speed shed from the rim in the reference frame of the rim. Based on the local dynamics of the ligament growth, Wang & Bourouiba (2022) derived and verified that the rate of momentum shed from the fluid ejected at speed, v_ℓ, can be approximated to be

$$\rho q_{out}(t) v_\ell(t) = \frac{1.34\pi}{We^{3/8}} \sigma r_s(t). \tag{6.6}$$

Using the scale of momentum change rate per radian as $\rho d_0^4/\tau_{cap}^2$, the dimensionless momentum shed from the rim per unit of time is

$$\dot{P}_{out}(T) = \frac{\dot{p}_{out}}{\rho d_0^4/\tau_{cap}^2} = Q_{out}(T)\dot{R}_s(T) + \frac{1.34\pi}{6We^{3/8}} R_s(T). \tag{6.7}$$

Using (3.7), (6.7) becomes

$$\dot{P}_{out}(T) = \sqrt{We}\left[Q_{out}(T)\dot{Y}_0(T) + \frac{1.34\pi}{6We^{3/8}} Y_0(T)\right]. \tag{6.8}$$

Wang & Bourouiba (2022) showed that the fluid speed v_ℓ shed from the rim in the reference frame of the rim is much smaller than the rim velocity $\dot{r_s}$. Thus, the contribution of the second term in the bracket of (6.8) is much smaller than the first term. For the intermediate-*We* range, $250 < We < 10^4$, over which common fragmentation processes

occur (Wang & Bourouiba 2022), the variation caused by We on the value of the bracket is within 10 %, a weak We-dependence. Without loss of generality, the Weber-dependent coefficient of the second term in the bracket can be approximated to take the average value in the intermediate-We range, $1.34\pi/(6We^{3/8}) \approx \pi/56$. Thus, the momentum partition of the fluid shed from the rim is approximately

$$\dot{P}_{out}(T) \approx \sqrt{We}\left[Q_{out}(T)\dot{Y}_0(T) + \frac{\pi}{56}Y_0(T)\right]. \tag{6.9}$$

Taking the integral of $\dot{P}_{out}$ with time, the cumulative momentum shed from the rim, which is transferred into the combination of ligaments and droplets, is thus

$$P_{out}(T) = \sqrt{We}\int_0^T \left[Q_{out}(T')\dot{Y}_0(T') + \frac{\pi}{56}Y_0(T')\right] \mathrm{d}T', \tag{6.10}$$

which, similar to P_{rim}, is also proportional to $\sqrt{We}$. Thus, the fraction of cumulative momentum shed from the rim at a given time T is

$$\frac{P_{out}(T)}{P_0} = \int_0^T \left[Q_{out}(T')\dot{Y}_0(T') + \frac{\pi}{56}Y_0(T')\right] \mathrm{d}T', \tag{6.11}$$

which is independent of the impact We.

Figure 11(b) shows the measured time evolution of the cumulative momentum fraction shed from the rim into the ligaments and droplets. At each time, the cumulative momentum is measured by accounting for the momentum of all ligaments along the rim and the cumulative momentum of secondary droplet shed up to that time. In addition, during the shedding, the growth of ligaments is restricted by surface tension. Thus, we also account for the momentum lost due to surface tension as part of the cumulative momentum shed from the rim. The experimental measurement of the cumulative momentum shed from the rim is thus

$$p_{out}^{(exp)}(t) = \sum_{n=1}^{N(t)} \rho\Omega_{ln}(t)u_{ln}(t) + \sum_{m=1}^{M(t)} \rho\Omega_{dm}(t)u_{dm}(t) + \int_0^t \sum_{n=1}^{N(t')} \frac{\pi}{2}\sigma w_n(t')\,\mathrm{d}t', \tag{6.12}$$

where $N(t)$ is the number of ligaments at time t, and $\Omega_{ln}(t)$ and $u_{ln}(t)$ are the volume and average velocity of the nth ligament at time t, respectively. Here, $N(t)$ is the total number of droplets shed at time t, while $M(t)$ is the total number of droplets shed by time t. The $\Omega_{dm}(t)$ and $u_{dm}(t)$ are the volume and velocity, respectively, of the mth droplet shed before time t. The $w_n(t)$ is the width of the nth ligament and $\pi\sigma w_n(t)/2$ is the surface tension force acting on that ligament at time t. All the quantities in (6.12) are measured with high precision by the AIP algorithms, as described in § 2.2.

Figure 11(b) shows that the measured time evolution of the cumulative momentum fraction in the fluid shed from the rim, in the form of ligaments and drops, (6.12), for different impact We. All data collapse on a single curve, which shows that the fraction of momentum in the fluid shed from the rim is indeed independent of We and is very well captured by our prediction (6.11) (solid line).

6.3. *Fraction of momentum in the sheet*

By analogy to the mass analysis in § 5, the momentum of the sheet, which includes both the part in the air and on the rod, is

$$p_s(t) = p_0 - p_{in}(t) \quad \text{with } p_{in}(t) = \int_0^t 2\pi\rho q_{in}(t')u(r_s, t')\,\mathrm{d}t', \tag{6.13}$$

which is the difference between the impacting drop momentum and the momentum entering the rim. Non-dimensionalized by the momentum scale per radian $\rho d_0^4/\tau^2$,

$$P_s(T) = \frac{p_s/2\pi}{\rho d_0^4/\tau_{cap}^2} = P_0 - P_{in}(T) \quad \text{with } P_{in}(T) = \int_0^T Q_{in}(T')U(R_s, T')\,\mathrm{d}T'. \tag{6.14}$$

Using the expression of $Q_{in}(T)$ (5.11), the sheet velocity profile $U(R_s, T) = R_s/T$ and the sheet radius of R_s (3.7), the cumulative momentum entering the rim $P_{in}(T)$ becomes

$$P_{in}(T) = \sqrt{We}\int_0^T \alpha\frac{\sqrt{\Phi(T')}}{T'}Y_0^2(T')\,\mathrm{d}T'. \tag{6.15}$$

The fraction of cumulative momentum entering the rim at time T is

$$\frac{P_{in}(T)}{P_0} = 12\sqrt{6}\int_0^T \alpha\frac{\sqrt{\Phi(T')}}{T'}Y_0^2(T')\,\mathrm{d}T', \tag{6.16}$$

which is independent of the impact We as verified by the data (figure 12*a*). It shows that the measured cumulative momentum entering the rim approaches the impacting drop momentum P_0, which shows that no momentum is lost in the sheet. The solid line in figure 12(*a*) shows that the prediction (6.16) captures the data at first order. However, a small but systematic offset from the data is observed. To understand the origin of the gap, we examine the rate of momentum injection into the rim per unit of time,

$$\dot{P}_{in}(T) = \alpha\sqrt{We}\frac{\sqrt{\Phi(T)}}{T}Y_0^2(T). \tag{6.17}$$

Figure 12(*b*) shows the momentum rate entering the rim for different We. Normalized by $\sqrt{We}$, all data collapse on a single curve and is well captured by our prediction (6.17) at late time. However, the prediction deviates slightly from the data at early time. This indicates that a second-order effect, not captured by our first-order sheet dynamics theory (Wang & Bourouiba 2022), takes place at early time. We leave to future work the deciphering of the physics underlying the early-time, second-order effect of the crushing of the drop.

Thus, the fraction of the momentum in the sheet with respect to the impacting drop momentum can be expressed as

$$\frac{P_s(T)}{P_0} = 1 - \frac{P_{in}(T)}{P_0} = 1 - 12\sqrt{6}\int_0^T \alpha\frac{\sqrt{\Phi(T')}}{T'}Y_0^2(T')\,\mathrm{d}T', \tag{6.18}$$

which is also independent of We as verified by the data (figure 13*a*), which is captured, at first order by our prediction (6.18). Note that given that the prediction (6.16) slightly underestimates the cumulative momentum, P_{in}, entering the rim from the sheet, the prediction (6.18) is expected to slightly overestimate the momentum in the sheet. These slight deviations arise from second-order effects at early crushing time, not captured by our sheet dynamics theory.

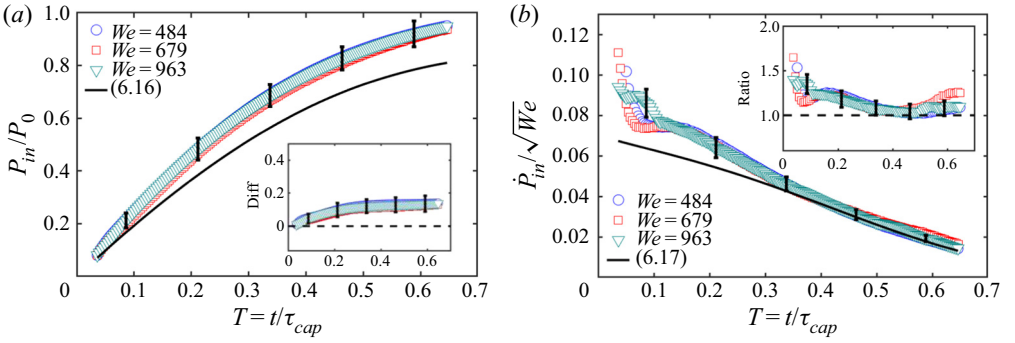

Figure 12. (*a*) Measured time evolution of the cumulative momentum fraction entering the rim from the sheet $P_{in}(T)/P_0$ for different impact *We*. All data collapse on a single curve, which shows the independence from *We*. The measured cumulative momentum entering the rim approaches the impacting drop momentum, which shows that no momentum is lost in the sheet. The solid line shows that the prediction (6.16) matches the data at first order, but with a slight underestimation. The inset shows the difference between the measured data and the prediction. (*b*) Measured time evolution of the rate of momentum fraction $\dot{P}_{in}$ entering the rim, which is proportional to $\sqrt{We}$. The solid line shows that the prediction (6.17) captures the data at first order, but with small underestimation at early time, which leads to the deviation of the prediction from the data in panel (*a*). The inset shows the ratio of measured data with prediction. Error bars indicate standard deviation across repeated experiments in each group.

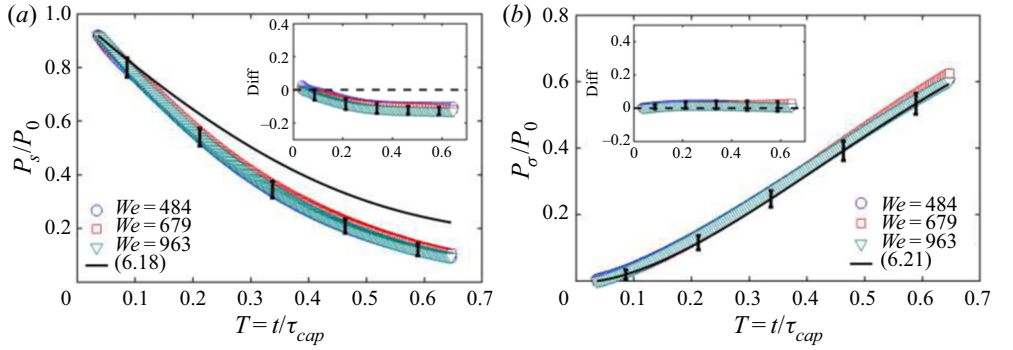

Figure 13. (*a*) Measured time evolution of the momentum fraction in the sheet P_s/P_0 for different *We*. All data collapse on a single curve showing independence from *We*. The prediction (6.18) (solid line) captures the data at first order, but with a slight overestimation, consistent with the underestimation of $P_{in}(T)/P_0$ in figure 12(*a*). (*b*) Measured time evolution of the cumulative surface tension force P_σ acting on the rim for different *We*, normalized by the impacting drop momentum P_0. All data collapse on a single curve, which shows independence from *We*, and is well captured by our prediction (6.21). Both insets show the difference between measured data and prediction. Error bars indicate the standard deviation across all repeated experiments in each group.

6.4. *Momentum balance across the sub-systems: sheet, rim and fluid shed*

We have now verified that the fractions of momentum in each sub-part of the fragmenting fluid system are independent of *We*. However, distinct from volume/mass partitioning, the sum of the momentum in each sub-part does not recover the impacting drop momentum, P_0. Instead, the total momentum summed over all sub-parts decreases over time due to surface tension forces acting on the rim, which reduces the momentum of the rim and the fluid shed from the rim. The cumulative surface tension force acting on the rim at a given

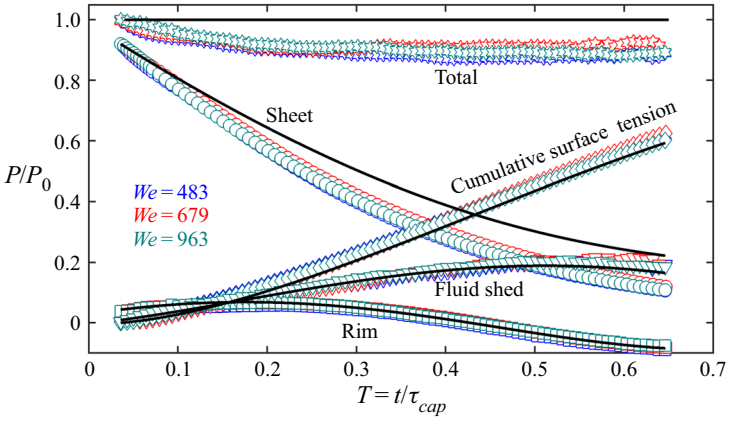

Figure 14. The partition of momentum fractions in each sub-part of the fluid system is independent of *We*. The small derivation of total momentum from unity originates from a second-order effect on the sheet dynamics at early time (as shown in figure 12*b*).

time t (impulse) is

$$p_\sigma(t) = \int_0^t 4\pi\sigma r_s(t')\,\mathrm{d}t', \tag{6.19}$$

and in non-dimensional form reads

$$P_\sigma(T) = \frac{p_\sigma/2\pi}{\rho d_0^4/\tau_{cap}} = \int_0^T \frac{1}{3}R_s(T')\,\mathrm{d}T' = \sqrt{We}\int_0^T \frac{1}{3}Y_0(T')\,\mathrm{d}T', \tag{6.20}$$

where (3.7) was used. The fraction of initial drop momentum, P_0, taken up by this force by time T is

$$\frac{P_\sigma(T)}{P_0} = \int_0^T 4\sqrt{6}Y_0(T')\,\mathrm{d}T', \tag{6.21}$$

which is also independent of *We* as verified by the data (figure 13*b*), and is very well captured by our prediction (6.21) (solid line in figure 13*b*).

Finally, figure 14 shows that, incorporating the impulse of the surface tension force, the total momentum recovers most of the initial momentum of the impacting drop at first order. In addition, the figure shows that the fractions of impacting drop momentum in each sub-part of the fluid system, as well as the cumulative impulse of the surface tension force, all follow universal time functions, which are independent of the impact *We* or energy.

7. Energy partitioning in each sub-part of the fluid system

We have determined that both the mass and momentum fractions in each sub-part of the fluid system are independent of impact *We*. We here turn to the energy. The total energy of the impacting drop includes its kinetic and surface energy, namely,

$$e_0 = e_0^k + e_0^s = \tfrac{1}{2}\rho\Omega_0 u_0^2 + \pi d_0^2\sigma, \tag{7.1}$$

which in non-dimensional form is

$$E_0 = \frac{e_0/2\pi}{\rho d_0^5/\tau_{cap}^2} = \frac{1}{12}\left(\frac{We}{12}+1\right) \approx \frac{We}{144}. \tag{7.2}$$

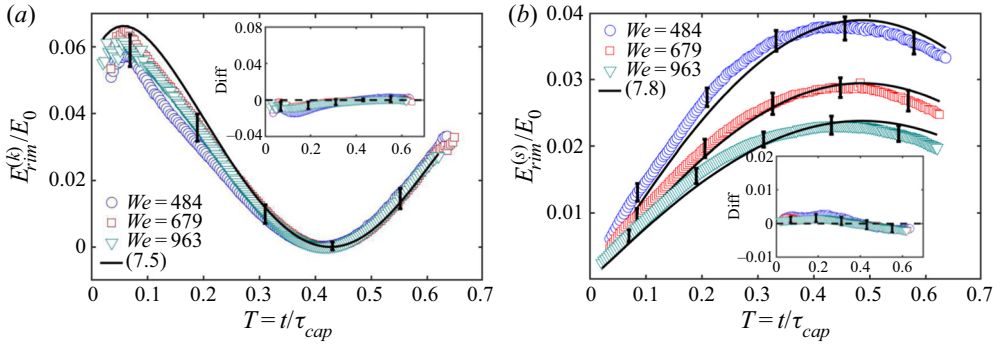

Figure 15. (*a*) Measured time evolution of the fraction of total energy taken up by the rim's kinetic energy $E^{(k)}_{rim}(T)/E_0$ for different impact *We*. All data collapse on a single curve showing independence from *We*. The solid line shows that our prediction (7.5) captures the data well. (*b*) Measured time evolution of the fraction of energy taken up by the rim's surface energy $E^{(k)}_{rim}(T)/E_0$, for different impact *We*. Contrary to the kinetic energy, the fraction of the rim's surface energy depends on the impact *We*, which is also captured well by our prediction (7.8). Both insets show that the difference between measured data and prediction remains zero, which indicates good agreement between the prediction and data. Error bars indicate the standard deviation across all repeated experiments in each group.

For the intermediate-*We* range $250 < We < 10^4$, where most common fragmentation occurs (Wang & Bourouiba 2022), the kinetic energy of the impacting drop is much larger than its surface energy. Thus, for the sake of brevity, we approximate the total energy of the impacting drop to its kinetic energy hereafter.

7.1. *Fraction of energy in the rim*

The energy of the rim can be separated into two parts, the kinetic energy and surface energy. Knowing the rim mass, m_{rim}, and velocity, $\dot{r}_s$, the rim kinetic energy is

$$e^k_{rim}(t) = \tfrac{1}{2}\rho\Omega_{rim}\dot{r}_s{}^2. \tag{7.3}$$

Thus, the non-dimensional form of this energy per unit radian reads

$$E^k_{rim}(T) = \frac{e^k_{rim}/2\pi}{\rho d_0^5/\tau_{cap}^2} = \frac{1}{2}We\left[\frac{\pi}{4}Y_0(T)\Psi^2(T)\right]\dot{Y}_0{}^2, \tag{7.4}$$

where (5.1), (3.7) and (4.4) were used. Equation (7.4) has an explicit dependence on impact *We*. When normalized by the impacting drop energy, E_0, the fraction of total energy taken up by the rim's kinetic energy is

$$\frac{E^k_{rim}}{E_0} = 18\pi[Y_0(T)\Psi^2(T)]\dot{Y}_0{}^2, \tag{7.5}$$

which is independent of impact *We* as verified by the data (figure 15*a*), and is very well captured by our prediction (7.5) (solid line).

Turning to the surface energy of the rim, consider the rim to have a cylindrical shape. Its surface energy is

$$e^s_{rim}(t) = 2\pi r_s(\pi b)\sigma. \tag{7.6}$$

In non-dimensional form, its surface energy per radian thus reads

$$E^s_{rim}(T) = \frac{e^s_{rim}/2\pi}{\rho d_0^5/\tau_{cap}^2} = \frac{\pi}{6}R_s B = \frac{\pi}{6}We^{1/4}[-6\ddot{Y}_0(T)]^{-1/2}Y_0(T), \tag{7.7}$$

where the expressions for the rim thickness B (4.4) and the sheet radius R_s (3.7) were used. Equation (7.7) has an explicit dependence on $We^{1/4}$.

When normalized by the total impact energy, E_0, the fraction of total energy stored in the rim's surface energy is

$$\frac{E^s_{rim}(T)}{E_0} = 24\pi We^{-3/4}[-6\ddot{Y}_0(T)]^{-1/2}Y_0(T), \tag{7.8}$$

which has an explicit dependence on $We^{-3/4}$ distinct from the energy fraction in the form of the rim's kinetic energy, which was shown to be independent of the impact We. Figure 15*b* shows the measured temporal evolution of the fraction of total energy in the rim's surface energy and shows that it is captured very well by our prediction (7.8). Comparing figures 15(*a*) and 15(*b*), the magnitude of the surface energy of the rim is approximately half that of the kinetic energy and accounts for less than 5 % of the total impacting drop energy. This confirms that the surface tension force and energy corresponding to the rim can be considered as negligible in the unsteady fragmentation.

Note that the effect of the surface energy of the rim was not reflected in the governing equation of the sheet radius (3.5). In fact, the surface tension force acting on the rim per radian, $2r_s\sigma$, given in the momentum balance equation (3.2) only corresponds to the surface energy of the evolving sheet. Analogous to the surface tension force of the capillary hydraulic jump problem (Bush & Aristoff 2003), the surface tension force corresponding to the surface energy of the rim, associated with the curvature of the rim, would scale as σb. It would thus have a distinct We-dependence from that of the dominant sheet surface tension force σr_s, as well as other terms in the governing equation (3.5) as confirmed in (7.8). Finally, given that for most impacts of interest $b \ll r_s$, this surface tension force corresponding to the rim's contribution is expected to be negligible.

7.2. *Fraction of energy in the fluid shed: ligaments and droplets*

Based on the rate of fluid volume shed from the rim, q_{out}, the rate of energy feeding the fluid shed, per radian, is

$$\dot{e}_{out}(t) = \tfrac{1}{2}\rho q_{out}(t)[\dot{r}_s(t) + v_\ell(t)]^2, \tag{7.9}$$

where $\dot{r}_s$ is the rim velocity and v_ℓ is the outflux speed shed from the rim. As mentioned in § 6, $\dot{r}_s$ is much larger than v_ℓ. Thus, the rate of kinetic energy passed on the fluid shed

is approximately

$$\dot{e}_{out}(t) \approx \tfrac{1}{2}\rho q_{out}(t)\dot{r_s}^2(t) + \rho q_{out}(t)v_\ell(t)\dot{r_s}(t). \tag{7.10}$$

Using the approximate expression for $\rho q_{out} v_\ell$, (6.6), gives

$$\dot{e}_{out}(t) \approx \frac{1}{2}\rho q_{out}(t)\dot{r_s}^2(t) + \frac{1.34\pi}{We^{3/8}}\sigma r_s(t)\dot{r_s}(t), \tag{7.11}$$

which in non-dimensionalized form reads

$$\dot{E}_{out}(T) = \frac{e_{out}}{\rho d_0^5/\tau_{cap}^3} = \frac{1}{2}Q_{out}(T)\dot{R_s}^2(T) + \frac{1.34\pi}{6We^{3/8}}R_s(T)\dot{R}_s(T). \tag{7.12}$$

As discussed in § 6.2, the Weber-dependent coefficient of the second term in the bracket can be approximated to take an average value in the intermediate-*We* range, which gives $1.34\pi/(6We^{3/8}) \approx \pi/56$. Thus, the energy of the fluid shed from the rim is approximately

$$\dot{E}_{out}(T) = \frac{e_{out}}{\rho d_0^5/\tau_{cap}^3} = \frac{1}{2}Q_{out}(T)\dot{R_s}^2(T) + \frac{\pi}{56}R_s(T)\dot{R}_s(T). \tag{7.13}$$

Using the expression of the sheet radius R_s, (3.7), gives

$$\dot{E}_{out}(T) = \frac{1}{2}We\left[Q_{out}(T)\dot{Y_0}^2(T) + \frac{\pi}{28}Y_0(T)\dot{Y}_0(T)\right]. \tag{7.14}$$

The cumulative fraction of total energy injected into the shed fluid at time T is thus

$$\frac{E_{out}(T)}{E_0} = \int_0^T 72\left[Q_{out}(T')\dot{Y_0}^2(T') + \frac{\pi}{28}Y_0(T')\dot{Y}_0(T')\right]\mathrm{d}T', \tag{7.15}$$

which is independent of the impact *We* as confirmed by our data (figure 16*a*). Here, experimental measurement of the cumulative kinetic energy shed from the rim is obtained from the measured volume rate, q_{out}, shed from the rim and the measured outflux speed v_ℓ using the AIP algorithms.

To confirm the accuracy of the measurements, the fluid shed from the rim becomes the ligaments and the cumulative secondary droplets. Thus, the total energy of the ligaments and the cumulative secondary droplets shed from the rim, including both the kinetic and surface energy, should be equal to the kinetic energy shed from the rim. Namely,

$$e_{out}(t) = \dot{e}^k_{drop}(t) + e^s_{drop}(t) + e^k_{liga}(t) + e^s_{liga}(t), \tag{7.16}$$

$$\text{with } e^k_{liga}(t) = \sum_{n=1}^{N(t)}\frac{1}{2}\rho\Omega_{ln}(t)u^2_{ln}(t), \quad e^s_{liga}(t) = \sum_{n=1}^{N(t)}\sigma A_{ln}(t), \tag{7.17a,b}$$

$$\text{and} \quad e^k_{drop}(t) = \sum_{m=1}^{M(t)}\frac{1}{2}\rho\Omega_{dm}(t)u^2_{dm}(t), \quad e^s_{drop}(t) = \sum_{n=1}^{N(t)}\sigma A_{dm}(t), \tag{7.18a,b}$$

where A_{ln} is the surface area of the nth ligament and A_{dm} is the surface area of the mth droplet. Other quantities were introduced in (6.12). Figure 16(*b*) shows the measured temporal evolution of the fraction of total energy in the ligaments and the cumulative droplets with respect to the impacting drop energy E_0. It shows that the total energy of the ligaments and droplets is very well captured by our prediction (7.15). Thus, the kinetic energy shed from the rim is indeed converted to the energy required for the formation of the ligaments and droplets. Note that matching also confirms the accuracy of our AIP algorithms.

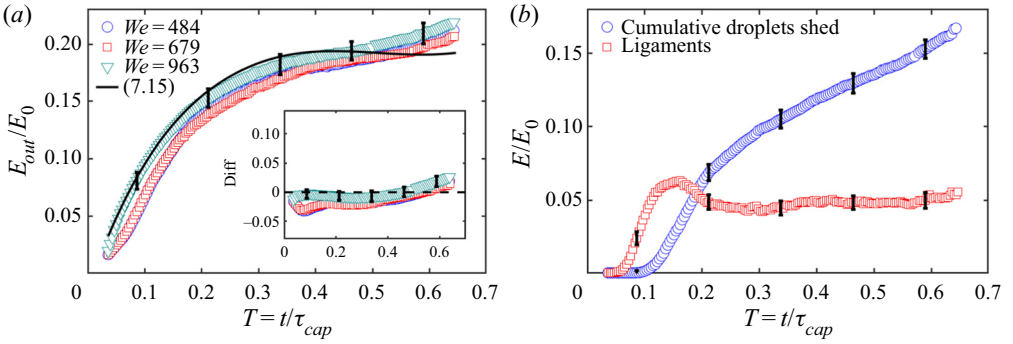

Figure 16. (*a*) Measured time evolution of the rate of kinetic energy of fluid shed from the rim for different impact *We* normalized by impact energy E_0. All data collapse on a single curve, which shows independence from *We*. The solid line shows that the prediction (7.15) captures the data well. The inset shows the difference between measured data and prediction remains zero, which indicates good agreement between prediction and data. (*b*) Measured time evolution of the fractions of total energy of the ligaments and total energy of the cumulative droplets shed over time, for $We = 679$. Error bars indicate the standard deviation across repeated experiments in each group.

7.3. *Fraction of energy in the sheet*

The energy of the sheet – both on the rod and in the air – includes two parts, the kinetic energy due to the fluid motion in the sheet and the surface energy. We will start with the kinetic energy. Similar to the mass and momentum of the sheet, the sheet kinetic energy can be evaluated as

$$e_s^{(k)}(t) = e_0 - e_{in}(t) \quad \text{with } e_{in}(t) = \int_0^t \frac{1}{2} 2\pi\rho q_{in}(t') u(r_s, t')^2 \, \mathrm{d}t', \tag{7.19}$$

which is the total impacting drop energy, e_0 in (7.1), minus the cumulative energy that has entered the rim at time t, $e_{in}(t)$. In non-dimensionalized form, it reads

$$E_s^{(k)}(T) = \frac{e_s/2\pi}{\rho d_0^5/\tau_{cap}^2} = E_0 - E_{in}(T) \quad \text{with } E_{in}(T) = \int_0^T \frac{1}{2} Q_{in}(T') U(R_s, T')^2 \, \mathrm{d}T'. \tag{7.20}$$

Using the expression of Q_{in} (5.11), the sheet velocity profile $U(R_s, T) = R_s/T$ and the sheet radius R_s (3.7), the cumulative energy entering the rim becomes

$$E_{in}(T) = We \int_0^T \frac{1}{2} \alpha \frac{\sqrt{\Phi(T')}}{T'^2} Y_0^3(T') \, \mathrm{d}T'. \tag{7.21}$$

Normalized by the impacting drop energy E_0,

$$\frac{E_{in}(T)}{E_0} = 72 \int_0^T \alpha \frac{\sqrt{\Phi(T')}}{T'^2} Y_0^3(T'), \, \mathrm{d}T', \tag{7.22}$$

which is independent of *We* as confirmed by the data (figure 17*a*). It shows that the measured cumulative energy entering the rim approaches that of the impacting drop energy, E_0, which shows that no energy is lost in the sheet prior to entering the rim. However, similar to the cumulative momentum entering the rim, a small systematic gap between the data and the prediction is observed accounting for approximately 15 % of the

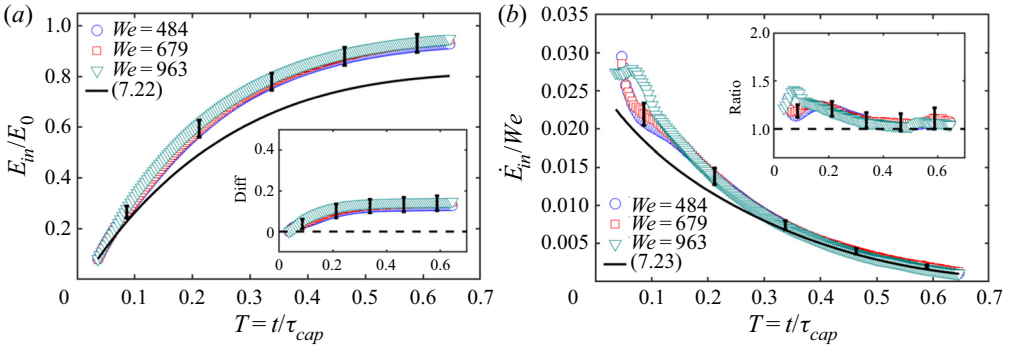

Figure 17. (*a*) Measured time evolution of the fraction of cumulative energy entering the rim from the sheet E_{in}/E_0 for different impact *We*. All data collapse on a single curve, which indicates independence from *We*. The measured cumulative energy entering the rim approaches to the impacting drop energy, which indicates no energy loss in the sheet. The solid line shows that the prediction (7.22) captures the data at first order, but with certain underestimation, consistent with that of the cumulative momentum P_{in}/P_0 entering the rim (figure 12*a*). The inset shows the difference between measured data and prediction. (*b*) Measured time evolution of the rate of energy injection into the rim $\dot{E}_{in}$, normalized by *We* to which $\dot{E}_{in}$ is proportional. The solid line shows that the prediction (7.23) deviates slightly from data at early time, which leads to the offset in panel (*a*). The inset shows the ratio of measured data with prediction. Error bars indicate the standard deviation across repeated experiments in each group.

total impacting drop energy E_0. To understand the origin of the gap, consider the energy entering the rim per unit of time:

$$\dot{E}_{in}(T) = We\frac{1}{2}\alpha\frac{\sqrt{\Phi(T)}}{T^2}Y_0^3(T), \tag{7.23}$$

which deviates from the data slightly at the early time (figure 17*b*). This is consistent with the cumulative momentum entering the rim (figure 12*b*), which confirms that a second-order effect, not captured by our first-order sheet dynamics (Wang & Bourouiba 2022) theory, takes place at early impact time.

Thus, the partition of the kinetic energy in the sheet with respect to the impacting drop energy becomes

$$\frac{E_s^{(k)}(T)}{E_0} = 1 - \frac{E_{in}(T)}{E_0} = 1 - 72\int_0^T \alpha\frac{\sqrt{\Phi(T')}}{T'^2}Y_0^3(T')\,\mathrm{d}T', \tag{7.24}$$

which is independent of *We* as confirmed by the data (figure 18*a*). Since the fraction of cumulative energy entering the rim is underestimated by 15 % (figure 17*a*), the kinetic energy in the sheet is overestimated by 15 % (figure 18*a*).

Taking a two-dimensional (2-D) horizontal sheet, the surface energy of the sheet is

$$e_s^{(s)}(t) = 2\sigma\pi(r_s)^2, \tag{7.25}$$

and in dimensionless form reads

$$E_s^{(s)} = \frac{e_s^{(s)}/2\pi}{\rho d_0^5/\tau_{cap}^2} = \frac{\sigma(r_s)^2}{\rho d_0^5/\tau_{cap}^2} = \frac{1}{6}R_s^2 = \frac{We}{6}Y_0^2(T), \tag{7.26}$$

where R_s (3.7) was used. Normalized by the impacting drop energy, E_0, (7.2),

$$\frac{E_s^{(s)}}{E_0} = 24Y_0^2(T), \tag{7.27}$$

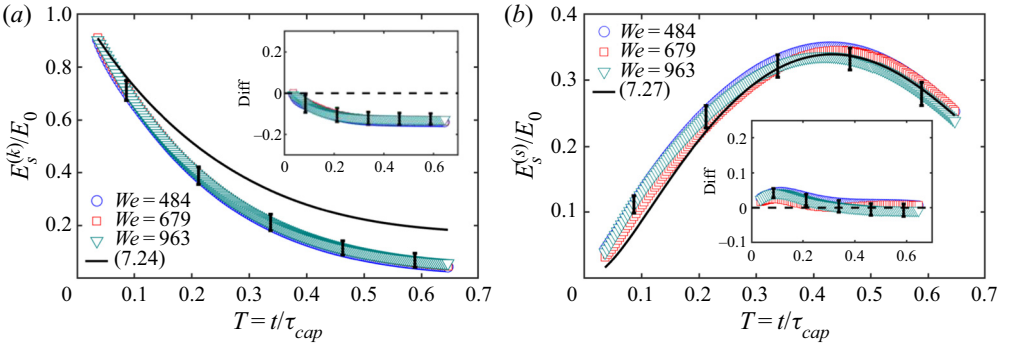

Figure 18. Measured time evolution of the fraction of energy in the sheet with its (*a*) kinetic energy, $E_s^{(k)}/E_0$, and (*b*) surface energy, $E_s^{(s)}/E_0$, for different impact *We*. All data collapse on a single curve, which indicates independence from *We*. The solid line in panel (*a*) shows that the prediction (7.24) captures the data at first order, but with certain overestimation, consistent with the underestimation of E_{in}/E_0 in figure 17(*a*). The solid line in panel (*b*) shows that the prediction (7.27) captures the data very well. Both insets show the difference between measured data and prediction. Error bars indicate the standard deviation across repeated experiments in each group.

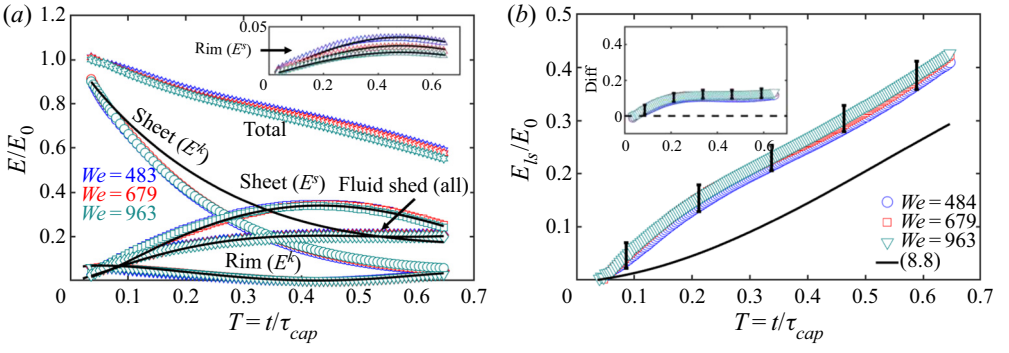

Figure 19. (*a*) The fractions of energy in each sub-part of the fluid system are all independent of *We*. (*b*) Measured time evolution of the energy loss in the system as shown in panel (*a*). The solid line shows the prediction (8.8) of energy loss in the rim, which accounts for 30 % of the original impacting drop energy. The remaining gap in predicted energy loss, of 15 %, in the system is due to a second-order mechanism occurring at early time (seen in figure 17*b*). The inset shows the difference between measured data and prediction. Error bars indicate the standard deviation across repeated experiments in each group.

which is also independent of *We* as confirmed by figure 18*b*. Thus, the energy fraction of the sheet, including both the kinetic and surface energy, is independent of *We*.

In sum, except for the surface energy of the rim, the fractions of energy in each sub-part of the system from sheet to rim to fluid shed are all independent of impact *We*, which is very well captured by our predictions (figure 19*a*). The rim surface energy contribution is less than 5 % of the impacting drop energy. Thus, the sum of the contributions of the energy of the sheet, rim and fluid shed remain mostly independent of impact *We* (figure 19*a*).

8. Energy dissipation throughout the unsteady fragmentation

In the above, we discovered that the fractions of energy in each sub-part of the system are independent of *We*. When summing all the contributions, we do not recover the total

impacting drop energy, with 45 % of the impacting drop energy lost (figure 19*a*). In this section we discuss where this takes place.

Recall that we found only a 15 % difference between the predicted energy contributions of each sub-part of the fluid system and the measurements, and that this difference originates from the early dynamics of the sheet (§ 7 and figures 17 and 18). To arrive at a gap of 45 % of total energy (figure 19*a*), we need to account for another 30 %.

First, considering the sheet on the rod, Wang & Bourouiba (2017) showed that the dynamics of the sheet is inviscid throughout its evolution, when the rod-to-drop size ratio, η, is within $1.4 < \eta < 1.9$. Indeed, in this range, the energy dissipation on the rod is negligible and Wang & Bourouiba (2017) verified that the cumulative energy leaving the edge of the rod throughout the entire dynamics recovers the impacting drop energy. Thus, the loss of energy shown in figure 19(*a*) does not occur on the rod for the regimes of $1.4 < \eta < 1.9$ impacts considered in this study.

Second, considering the sheet in the air, the energy is also conserved. Wang & Bourouiba (2017) showed experimentally and validated that the sheet is governed by an inviscid equation with an inviscid velocity profile, $u(r, t) = r/t$, followed by each fluid parcel emanating from the edge of the rod, moving radially in the sheet at constant speed. Note that a demonstration of energy conservation in the sheet is given in Appendix B.1

Given that energy is conserved on the rod and in the sheet in the air, and that the energy of the fluid shed from the rim is all converted to the total energy of the ligaments and droplets, as shown in figure 16(*a*), thus loss of energy can only be accounted for in the rim. In the prior literature, Taylor (1959) and Culick (1960) studied steady sheet evolution under capillary forces and discovered that the governing equation for the sheet radius, or rim velocity, is based on a momentum balance at the rim, rather than an energy balance, the two approaches leading to discrepancy of the order of a factor of $\sqrt{2}$ for the prediction of the retraction speed. By analogy, for unsteady sheet evolution, Wang & Bourouiba (2022) derived the governing equation for the sheet radius based on momentum balance at the rim as well. To discuss the implications of this momentum balance, we here attempt to quantify the loss of energy implied by the corresponding momentum balance used.

An intuitive approach to predict the energy loss in the rim is to consider the dynamics in the moving reference frame of the rim. In the non-Galilean reference frame of the decelerating rim, the rim is stationary, but subjected to a fictitious force associated with the rim's inertia $m\ddot{r}_s$. The energy entering the rim per unit of time becomes

$$\dot{e}_{in}^{(r)} = \tfrac{1}{2}\rho(2\pi r_s)h(r_s, t)[u(r_s, t) - \dot{r}_s]^3. \tag{8.1}$$

Given that obviously the rim is fixed in the moving reference frame of the rim, its kinetic energy and the work done by the capillary force and the fictitious force on the rim are both null. Thus, the energy lost in the rim per unit of time is simply $\dot{e}_{in}^{(r)}$, the energy entering the rim per unit of time in the same reference frame, namely

$$\dot{e}_{ls} = \dot{e}_{in}^{(r)} = \tfrac{1}{2}\rho(2\pi r_s)h(r_s, t)[u(r_s, t) - \dot{r}_s]^3 = \tfrac{1}{2}\dot{m}[u(r_s, t) - \dot{r}_s]^2. \tag{8.2}$$

Physically, $\dot{e}_{ls}$ originates from the energy loss due to the sudden reduction of fluid speed upon fluid rim entry. Indeed, prior to entering the rim, the fluid parcel speed is $u(r_s, t)$, while it becomes the rim's speed when reaching the rim, $\dot{r}_s$, with a leading sudden speed reduction $\Delta u = u(r_s, t) - \dot{r}_s$. Thus, over each unit of time, the associated energy loss is

$$\dot{e}_{ls} = \tfrac{1}{2}\dot{m}\Delta u^2 = \tfrac{1}{2}\dot{m}[u(r_s, t) - \dot{r}_s]^2, \tag{8.3}$$

which recovers what we derived in (8.2). In sum, we recover that the energy loss is indeed in the rim due to the sudden velocity reduction when a fluid parcel enters the rim from

the sheet. Note that a more complete demonstration of energy loss at the rim is given in Appendix B.2.

Having quantified the energy loss in the rim without shedding, the energy loss in the rim with shedding can be directly expressed in the reference frame of the rim as

$$\left.\begin{aligned} \dot{e}_{ls} = \dot{e}_{in}^{(r)} - \dot{e}_{out}^{(r)} = \frac{1}{2}\rho(2\pi q_{in})[u(r_s,t) - \dot{r}_s]^2 - \frac{1}{2}\rho(2\pi q_{out})v_\ell^2, \\ \text{with } q_{in} = h(r_s,t)r_s[u(r_s,t) - \dot{r}_s] \text{ and } q_{out} = q_{in} - \frac{\mathrm{d}}{\mathrm{d}t}\left(\frac{\pi}{4}b^2 r_s\right). \end{aligned}\right\} \tag{8.4}$$

Wang & Bourouiba (2022) showed that the relative velocity of fluid entering the rim $u(r_s,t) - \dot{r}_s$ is approximately four times larger than the outflux speed v_ℓ in the reference frame of the rim, and that the rate of fluid volume entering the rim, q_{in}, per radian, is also systematically larger than the rate of fluid volume shed from the rim, q_{out}. The second term contribution in (8.4) is less than 5 % of the first term, thus negligible. Hence, the energy loss in the rim per unit of time accounting for continuous shedding reads

$$\dot{e}_{ls} = \tfrac{1}{2}\rho(2\pi q_{in})[u(r_s,t) - \dot{r}_s]^2 \quad \text{with } q_{in} = \rho(2\pi r_s)h(r_s,t)[u(r_s,t) - r_s]. \tag{8.5}$$

In non-dimensional form, (8.5) can be simplified to read

$$\dot{E}_{ls}(T) = \frac{\dot{e}_{ls}/2\pi}{\rho d_0^5/\tau_{cap}^3} = \frac{1}{2}Q_{in}(T)\left[\frac{R_s(T)}{T} - \dot{R}_s(T)\right]^2 = \frac{\alpha^2}{2}\frac{Q_{in}(T)}{H(R_s,T)}, \tag{8.6}$$

where the sheet velocity profile $U(R_s,T) = R_s/T$ and the non-Galilean Taylor–Culick law (5.10) were used. Here, $\alpha = \sqrt{(2-\pi/7)/6}$ defined in (5.10). Using (4.3) and (5.11) gives

$$\dot{E}_{ls}(T) = \frac{\alpha^2}{2}We\frac{\alpha\sqrt{\Phi(T)}Y_0(T)}{\Phi(T)} = \frac{\alpha^3}{2}We\frac{Y_0(T)}{\sqrt{\Phi(T)}}. \tag{8.7}$$

The fraction of initial energy ending up being lost in the rim, over time T, reads

$$\frac{E_{ls}(T)}{E_0} = 72\int_0^T \alpha^3\frac{Y_0(T')}{\sqrt{\Phi(T')}}\,\mathrm{d}T. \tag{8.8}$$

The solid line in figure 19(*b*) shows that the prediction (8.8) of loss in the rim accounts for up to 30 % of the original impact drop energy, E_0. Given that the full energy loss of the system is 45 % (figure 19*a*) of the original energy, the remaining 15 % is in fact consistent with the deviation between the theoretical and measured energy in the sheet (figure 18*a*). Here, we note that the measured cumulative energy, E_{in}, entering the rim approaches that of the impacting drop energy, E_0, (figure 17*a*). Thus, the 15 % energy is neither lost from surface stresses on the surface nor in the sheet in the air, but at the entrance of the rim due to a second-order mechanism pertaining to the early time of impact, not captured by our theory focused on the dynamics on the order of the capillary time.

In sum, we note that the above analysis enabled us to elucidate the regions and times of energy loss in this canonical sheet-mediated unsteady fragmentation. Most of which (30 %) is lost in the rim continuously, while a smaller portion (15 %) is due to early impact dynamics. Nevertheless, this approach cannot identify the exact physical mechanism responsible for the energy loss at the rim. This can be captured by a combination of regular shear viscosity dissipation, eddy viscosity or just the conversion of forward one-dimensional (1-D) momentum into three-dimensional circulation within the rim,

none of which are captured by our 1-D model of the radial dynamics, which ignores, by construction, the detailed physics in the control volume, i.e. the rim. Elucidating the exact mechanism(s) of dissipation in the rim and their relative contributions would require detailed local quantifiable flow visualizations of the dynamics in the rim revealing the key ingredients of this unsteady nonlinear system.

9. Robustness of the inviscid unsteady partition theory

9.1. *Comparison with the experiments using fluids of various properties*

To verify the robustness of our prediction of partition of volume/mass, momentum and energy, in unsteady fragmentation, we conducted experiments using fluids of different properties (table 2). We used glycerol–water mixtures to vary the fluid viscosity and DMSO to vary the fluid surface tension. As shown in §§ 4–7, all predictions are derived based on the $Bo = 1$ criterion that governs the rim dynamics (§ 3.1) and the non-Galilean Taylor–Culick law that governs the sheet dynamics (§ 3). These two conditions hold for impact We and Re that are much larger than unity so as to ensure early onset of shedding and inviscid regimes of sheet dynamics, respectively. Regarding the regime of validity of the $Bo = 1$ criterion for rim thickness self-adjustment, we showed in prior work that it is robust for local rim Re : $\widehat{Re} = \sqrt{\sigma b/\rho\nu^2} < 6\sqrt{2}$ (Wang *et al.* 2018).

For low-impact We, the rim thickness $B \sim We^{-1/4}$ (4.4) becomes thicker. Thus, the capillary time of the rim $\tau_b = \sqrt{\rho b^3/8\sigma}$, characteristic of rim destabilization, increases, which results in the delays of fluid shedding from the rim. Riboux & Gordillo (2015) showed that rim destabilization ceases when the ratio of the rim capillary time to the rim-thickening time $\tau_h = b/\dot{b}$ is larger than 0.1, namely $\tau_b/\tau_h > 0.1$, where the $Bo = 1$ criterion is also violated.

Figure 20(a) compares snapshots of unsteady sheet fragmentation upon impact of a drop of water, DMSO and glycerol (50 %)–water (50 %) mixture at the time of maximum sheet radius $T_m = 0.43\tau_{cap}$. This comparison shows no qualitative difference in fragmentation patterns. The impact conditions for all three fluids lie in the regime $\widehat{Re} = \sqrt{\sigma b/\rho\nu^2} > 6\sqrt{2}$ where the $Bo = 1$ criterion holds, as confirmed in the inset of figure 20(b). The time evolution of sheet radius for all three fluids also follows the non-Galilean Taylor–Culick law (figure 20b). Figure 20(b) shows the time evolution of the volume fractions of fluid in the sheet, in the rim and shed from the rim throughout the entire fragmentation for the three different fluids. For each quantity, the data of all three fluids collapse on a single curve and are well captured by our prediction (solid lines), which confirms the robustness of our prediction for the partition of unsteady fragmentation as long as $Bo = 1$ (3.1) and the non-Galilean Taylor–Culick law of sheet expansion are both satisfied.

9.2. *Regime map in terms of We and Re where the partition theory holds*

When fluid viscosity is sufficiently large for the local Reynolds number of the rim to satisfy $\widehat{Re} < 6\sqrt{2}$, droplet shedding ceases throughout the entire sheet evolution. Figure 21(a) compares the unsteady fragmentation phenomena upon drop impact for increasing fluid viscosity. As seen in the figure for the glycerol (70 %)–water (30 %) mixture, the cumulative volume fraction, Ω_{out}/Ω_0, of fluid shed from the rim becomes systematically smaller than that of the other two lower viscosity mixtures used. We note that the sheet radius normalized by $\sqrt{We}$ for the glycerol (70 %)–water (30 %) mixture is systematically smaller than that for the other lower viscosity cases. This is not due to suppression

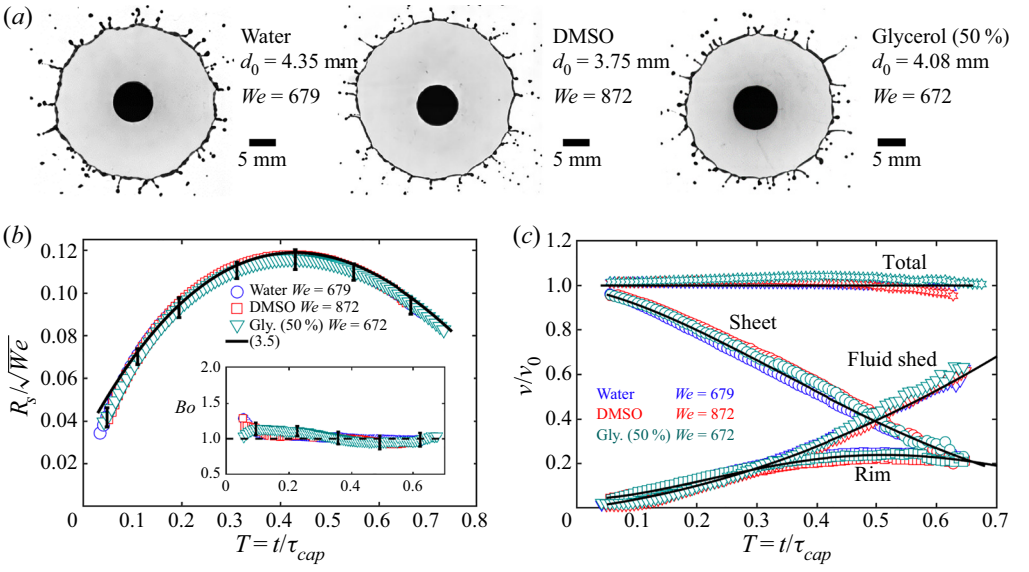

Figure 20. (*a*) Comparison of snapshots of unsteady fragmentation upon drop impact using three fluids (water, DMSO and glycerol (50 %)–water (50 %) mixture) at the time of maximum sheet radius $T_m = 0.43\tau_{cap}$. It shows no notable difference in fragmentation phenomenology. Full details of impact conditions and fluid properties for each fluid are given in tables 1 and 2. (*b*) Measured time evolution of the sheet radius throughout the entire fragmentation for different fluids is well captured by the non-Galilean Taylor–Culick law (3.5). The inset shows that the rim thickness for different fluids follows the $Bo = 1$ criterion (3.1). Error bars indicate the standard deviation across all repeated experiments for each group. (*c*) Measured time evolution of the volume fractions in different sub-parts of the system during fragmentation for different fluids. For each sub-part, the data for different fluids collapse on a single curve, and are well captured by the prediction, which indicates robustness of the theory.

or reduction of shedding. The reduction of fluid shedding would in fact increase the maximum radius of the sheet (Wang & Bourouiba 2022) due to less momentum and mass losses from the rim (figure 21*b*). However, viscous surface stresses $\tau \sim \mu \frac{\mathrm{d}u}{\mathrm{d}z}$ on the rod surface increases with μ, which result in the reduction of the momentum entering the rim in the first place. We can confirm support for this effect with the departure of the sheet thickness and velocity profiles form the inviscid limit as well. Here, $u(r, t)$ is the sheet velocity profile and z is the direction along the sheet thickness.

Systematic experimental results shown in figures 20 and 21 confirm that the We independence of partitioning of the volume/mass, momentum and energy in each sub-part of the fragmentation system holds if and only if the $Bo = 1$ criterion holds at the rim and the sheet radius continues to be governed by the non-Galilean Taylor–Culick law, where viscous effects are negligible. Recall that the validity of the rim's $Bo = 1$ criterion is for $\widehat{Re} > \widehat{Re}_c = 6\sqrt{2}$ (Wang *et al.* 2018). For the rim's local $Bo = 1$ to be ensured,

$$\widehat{Re}_{min} = \frac{\sqrt{\rho\sigma b_{min}}}{\mu} > \widehat{Re}_c = 6\sqrt{2} \tag{9.1}$$

has to hold, where b_{min} is the minimum thickness of the rim during the fragmentation. Physically, the rim thickness should grow from zero at the very beginning of the impact. The fluid emanating from the sheet rapidly thickens the rim. Thus, it is reasonable to use the asymptotic value of the rim thickness at $t = 0$, derived based on the $Bo = 1$ criterion (4.4), as the minimum rim thickness during fragmentation (thickness increases over time

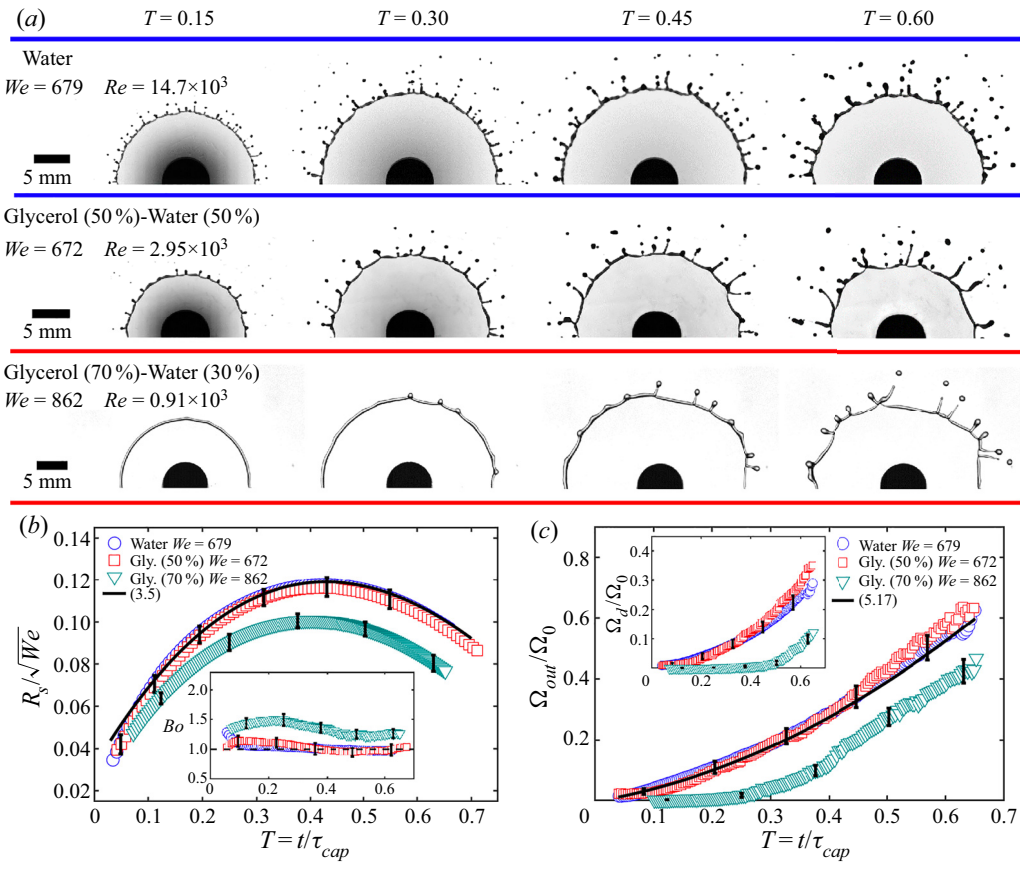

Figure 21. (*a*) Comparison of sequential snapshots from unsteady fragmentation upon drop impact using fluids from low to high viscosity. Fragmentation in the most viscous case is clearly reduced compared with the less viscous cases. (*b*) Measured time evolution of the sheet radius for the three cases is shown in panel (*a*). The radii temporal evolution collapse for the two fluids of lower viscosity. Viscous effects clearly start affecting the sheet radius evolution in the third case. The inset shows that data for the first two cases follow the $Bo = 1$ criterion (3.1), while the data for the third case do not. (*c*) The evolution of the volume fractions of fluid shed from the rim remains essentially inviscid, matching the prediction (5.17) assuming a non-Galilean Taylor–Culick law of evolution of the sheet and the rim's $Bo = 1$ criterion, the volume fractions shed from the rim collapse on a single curve, while the impact for the fluid of higher viscosity clearly deviates and shows a smaller cumulative shedding. Error bars indicate the standard deviation across all repeated experiments for each group.

as seen in figure 6*b*), which gives

$$b_{min} = 0.2We^{-1/4}d_0. \tag{9.2}$$

Substituting (9.2) into (9.1) gives

$$\widehat{Re}_{min} = \frac{\sqrt{0.2\rho\sigma d_0}}{\mu}We^{-1/8} = \sqrt{0.2}ReWe^{-5/8} > 6\sqrt{2}. \tag{9.3}$$

Thus, the regime of validity of the local instantaneous $Bo = 1$ rim criterion reads

$$ReWe^{-5/8} > \frac{6\sqrt{2}}{\sqrt{0.2}} \approx 19.0. \tag{9.4}$$

Having quantified the effect of viscosity on the partition theory of unsteady fragmentation, we shift our focus to the effect of impact *We* on the fragmentation. Figure 22(*a*) compares the sheets and fragments upon drop impact for different impact *We*. As the impact *We* decreases, fluid continues to be shed from the rim for $We > 250$, where the $Bo = 1$ holds (inset of figure 22*b*) and the sheet radius follows the non-Galilean Taylor–Culick law (figure 22*b*). However, for *We* as low as 170, both the $Bo = 1$ criterion and the non-Galilean Taylor–Culick law no longer hold (inset of figure 21*b*). Consequently, the cumulative volume fraction, Ω_{out}/Ω_0, of fluid shed from the rim becomes systematically smaller than that of the $We > 250$ regime (figure 22*b*). However, the reduction of fluid shed from the rim for low *We* is not due to viscous effects. For $We = 170$, from table 2, we have that

$$ReWe^{-5/8} \approx 297 \gg 19, \tag{9.5}$$

which satisfies the criterion (9.4) for a negligible viscous effect. The absence of shedding, which leads to a violation of the rim's $Bo = 1$ criterion, is at play here. This violation is associated with a rim thickening that delays its destabilization: as *We* decreases, the rim thickness $B \sim We^{-1/4}$ increases, leading to the increase of the rim capillary time, $\tau_b = \sqrt{\rho b^3/8\sigma}$, which delays rim destabilization and associated shedding into droplets. Furthermore, Riboux & Gordillo (2015) showed that instead of merely delaying rim destabilization and droplet ejection, droplet ejection ceases when the ratio of the rim capillary time to rim-thickening time becomes larger than 0.1, i.e. $\tau_b/\tau_h > 0.1$. Choosing the characteristic length scale to be d_0, and the characteristic time scale $\tau_{cap} = \sqrt{\rho d_0^3/6\sigma}$, this rim stabilization criterion reads

$$\frac{\tau_b}{\tau_h} = \dot{b}\sqrt{\frac{\rho b}{8\sigma}} = \dot{B}\sqrt{\frac{3}{4}B} > 0.1. \tag{9.6}$$

When the rim destabilization is impeded, no fluid is shed from the rim: the rim thickness *B* used in (3.1) is no longer determined by the local instantaneous $Bo = 1$, but by mass conservation at the rim, namely,

$$\frac{\mathrm{d}}{\mathrm{d}t}\left(\frac{\pi}{4}\tilde{b}^2 r_s\right) = q_{in}(t) = h(r_s, t)(u(r_s, t) - \dot{r}_s)r_s(t), \tag{9.7}$$

recalling that $q_{in}(t)$ is the volume rate entering the rim per unit radian, $r_s(t)$ is the sheet radius, and $u(r_s, t)$ and $h(r_s, t)$ are the sheet velocity and thickness profiles (Wang & Bourouiba 2017). We denote the rim thickness b (4.4) determined by the $Bo = 1$ criterion, while we denote the rim thickness derived from mass conservation at the rim as $\tilde{b}$. The sheet radius $r_s(t)$ used in (9.7) should be based on the sheet dynamics assuming no shedding from the rim. However, for simplicity, we continue to use the prediction of $r_s(t)$ (3.8) based on the non-Galilean Taylor–Culick law to estimate the rim thickness with no shedding at first-order correction. Taking the characteristic length scale d_0 and time scale $\tau_{cap} = \sqrt{\rho d_0^3/6\sigma}$, the rim thickness without shedding, in non-dimensional form, reads

$$\tilde{B}(T) = \left\{\frac{4}{\pi R_s(T)}\int_0^T Q_{in}(T')\,\mathrm{d}T'\right\}^{1/2} = \left\{\frac{4}{\pi R_s(T)}\mathcal{V}_{in}(T)\right\}^{1/2}, \tag{9.8}$$

where $V_{in}(T)$ is the cumulative volume entering the rim per unit radian as derived in (5.12). Figure 23(*a*) shows the time evolution of the rim thickness for $We = 170$ where

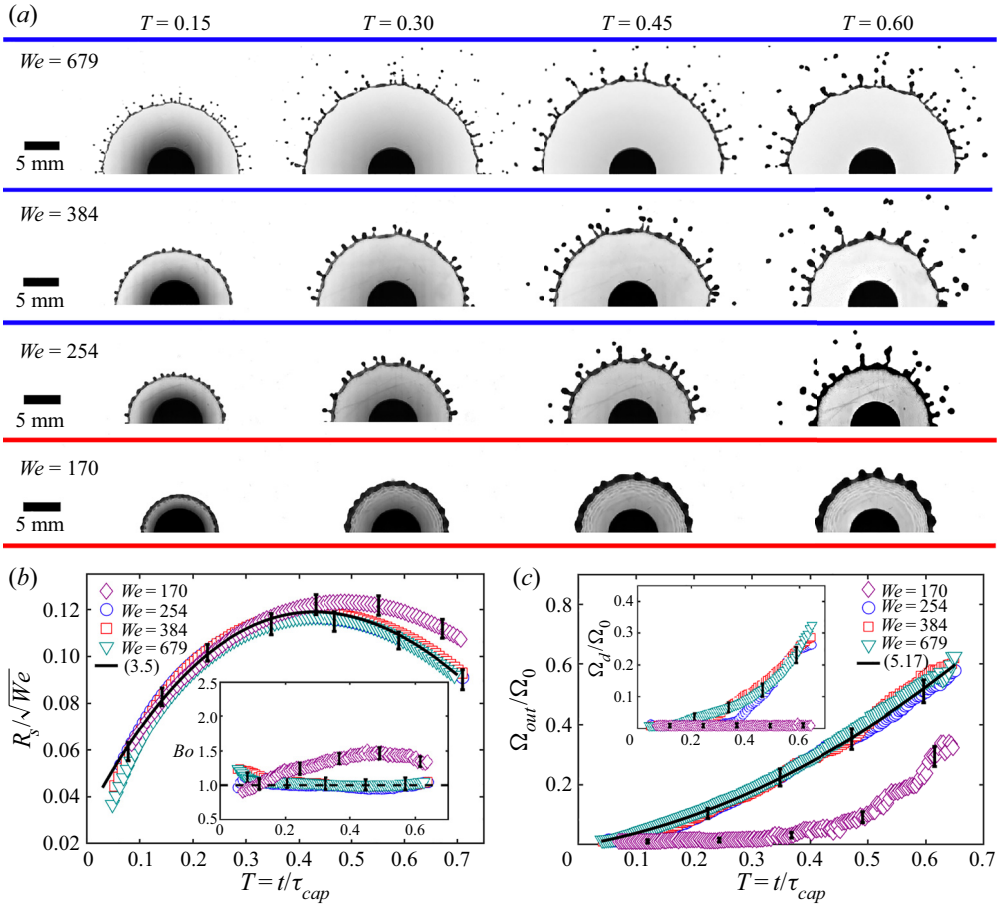

Figure 22. (*a*) Sequential snapshots of sheet upon drop impact for different impact *We*. Droplet shedding during sheet expansion takes place as long as $We > 170$. (*b*) Measured time evolution of sheet radius for the four cases shown in panel (*a*). Data for all cases of $We > 250$ collapse on a single curve and are well captured by the non-Galilean Taylor–Culick law (3.5). Data for $We = 170$ deviate. The inset shows that data for all cases of $We > 250$ continue to follow the $Bo = 1$ criterion (3.1), while the data for $We = 170$ do not. (*c*) Measured time evolution of the volume fractions of fluid shed from the rim. For all cases of $We > 250$ where the sheet radius follows the non-Galilean Taylor–Culick law and the rim follows the $Bo = 1$ criterion, the volume fractions shed from the rim collapse on a single curve and are well predicted by (5.17). However, for $We = 170$, the volume fraction of fluid shed from the rim (including the cumulative droplet volume seen in the inset) are systematically smaller than those for $We > 250$. Error bars indicate the standard deviation across all repeated experiments for each group.

no fluid is shed from the rim. Using $R_s(T)$ (3.8) and $V_{in}(T)$ (5.12), the prediction of rim thickness omitting shedding matches the experiments best, compared with the prediction based on the shedding-conditional rim's $Bo = 1$ criterion. Since $V_{in}(T)$ is independent of the impact *We* and the sheet radius $R_s(T) = \sqrt{We}Y_0(T)$, the rim thickness $\tilde{B}(T)$ based on mass conservation at the rim also shows

$$\tilde{B}(T) = \frac{1}{We^{1/4}}\Theta(T) \quad \text{with } \Theta(T) = \left\{\frac{4}{\pi Y_0(T)}\mathcal{V}_{in}(T)\right\}^{1/2}, \tag{9.9}$$

which scales as $We^{-1/4}$, consistent with the rim thickness $B(T)$ (3.1) based on the $Bo = 1$ criterion as discussed in § 4. Here, $\Theta(T)$ is a universal function independent of the

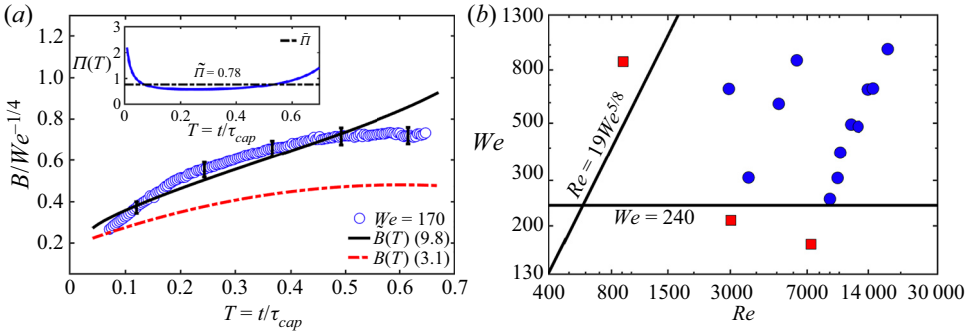

Figure 23. Measured time evolution of the rim thickness for $We = 170$ for which the fluid shed from the rim ceases. The prediction of $\tilde{B}(T)$ (9.8) based on mass conservation at the rim (solid line) matches the data better than the prediction of $B(T)$ (3.1) based on the $Bo = 1$ criterion (dash line). The inset shows the time evolution of the function $\Pi(T)$ (9.10) which remains approximately constant. (*b*) Phase diagram of the regime where the *We* independence property of partitioning of volume, mass, momentum and energy in each sub-part of the unsteady fragmentation system holds. The solid lines show the theoretical prediction for the boundary of the regime.

impact *We*. Substituting (9.9) into (9.6) gives

$$\frac{1}{We^{3/8}}\Pi(T) > 0.1 \quad \text{with } \Pi(T) = \Theta(T)\sqrt{\frac{3}{4}\dot{\Theta}(T)}, \tag{9.10}$$

where $\Pi(T)$ is independent of the impact *We*. The inset of figure 23(*a*) shows the time evolution of $\Pi(T)$ based on the prediction of $\Theta(T)$ (9.9). Except at very early time $T < 0.05\tau_{cap}$, $\Pi(T)$ remains approximately constant during the entire evolution. Without loss of generality, we take the time average of $\Pi(T)$, which gives $\bar{\Pi} = 0.78$ (inset of figure 23*a*). Substituting $\bar{\Pi} = 0.78$ into (9.10), the criterion for the regime where the rim thickening prohibits fragmentation can be re-expressed in terms of the impact *We* as

$$We^{3/8} < \frac{\bar{\Pi}}{0.1} = 7.8 \Longrightarrow We < We_c = 7.8^{8/3} \approx 240, \tag{9.11}$$

which is consistent with the experiments shown in figure 22, and also the upper boundary ($We = 250$) of the lower Weber regime (Wang & Bourouiba 2022).

Using all the above, we construct a regime diagram (figure 23*b*), which shows the phase diagram in terms of impact *We* and *Re* for the regime where the predictions of partitioning and their *We* independence hold. The blue circles indicate the experiments that follow the prediction, while the red squares represent the experiments that do not. The theoretical boundaries derived based on the viscous effect (9.4) and rim-thickening effect (9.10) are shown. They capture the boundaries of the experiments well. The boundaries of this regime of validity are determined by $ReWe^{-5/8} > 19$ for which the viscous effect at the rim is negligible and $We > 240$ for which the rim-thickening effect on the rim destabilization is negligible.

10. Conclusion

We presented the results of a combined theoretical and experimental investigation of how the volume/mass, momentum and energy transfers from the sheet, to rim to fluid shed from the rim during a canonical unsteady sheet fragmentation upon drop impact

on a surface of comparable size to that of the impacting drop. We combined the non-Galilean Taylor–Culick law that governs the sheet evolution in the air, the unified velocity and thickness profile of the sheet, and the universal rim destabilization that leads to a self-adjustment of the rim's thickness to maintain a $Bo = 1$ criterion to predict and validate thes temporal evolution of mass/volume, momentum and energy in each sub-part of the fragmentation system: from sheet, to rim to fluid shed. All predictions are derived without fitting parameters and validated against detailed measurements done with especially developed advanced image processing algorithms that enabled measurement with unprecedented precision.

We derived and verified experimentally that the temporal evolution of the fraction of volume/mass of the fluid shed from the rim during the entire unsteady fragmentation is in fact independent of impact *We* or energy (§ 5.2 and figure 9*b*). In addition, the temporal evolutions of the fractions of volume/mass (§ 5 and figure 10*b*), momentum (§ 6 and figure 14) and energy (§ 7 and figure 19*a*) in each sub-part of the system are also independent of impact conditions: over the same dimensionless time interval, the volume/mass, momentum and energy redistribute among the sheet, the rim and the fluid shed in a manner that is indifferent to the impact energy.

The detailed analysis of the partition of volume/mass, momentum and energy enabled us to clarify the energy dissipation and the interplay between the complementary insights gained from energy and momentum analyses of this fluid system (§ 8). We showed that a loss of 45 % of the original impact energy occurs regardless of impact energy (figure 19). An energy loss of 30 % occurs universally in the rim upon the rapid deceleration of fluid parcels that continuously enter the rim from the sheet, while the remaining 15 % is lost in the early dynamics of the sheet formation, on a time scale of the order of the impact time scale. We confirm that these losses are not due to stresses on the surface on which the drop impacts; what physical mechanism causes this loss remains a open question.

We showed that the time evolution of volume, momentum and energy partitioning in each sub-part of the unsteady fragmentation system examined here, is robust to change of fluid properties in the inviscid and inertia-dominated limits of impacts. We showed that if and only if the rim's $Bo = 1$ criterion holds with the non-Galilean Taylor–Culick law governing the sheet dynamics, the partitioning of volume, momentum and energy in each sub-part is independent of *We* and associated impact conditions. In terms of the impact *We* and *Re*, the criterion for negligible viscous effects at the rim is derived as $ReWe^{-5/8} > 19$ and the criterion for negligible thickening effect at the rim is $We > 240$. These two predicted criteria form the boundaries of the regime where the partition law holds and captures the experimental data. Outside of these ranges of *We*–*Re* values, with *Re* and *We* that are too low, viscous (Wang & Bourouiba 2018*a*) and thickening effects (Agbaglah *et al.* 2013; Riboux & Gordillo 2015) at the rim can mitigate rim destabilization, prohibiting fluid shedding from the rim, which violates the $Bo = 1$ criterion.

In sum, in this study, we elucidated the core physical constraints and associated universal laws of temporal evolution and partitioning of volume/mass, momentum and energy in unsteady sheet-mediated fragmentation. The results provide a quantitative benchmark for robust validation of models for a large class of atomization and spray processes from unsteady sheets and impacting drops. The fundamental insights gained are critical for the accurate modelling of sheet-mediated fragmentation, important for prediction, control and optimization of sprays in a wide range of health, environmental and industrial applications.

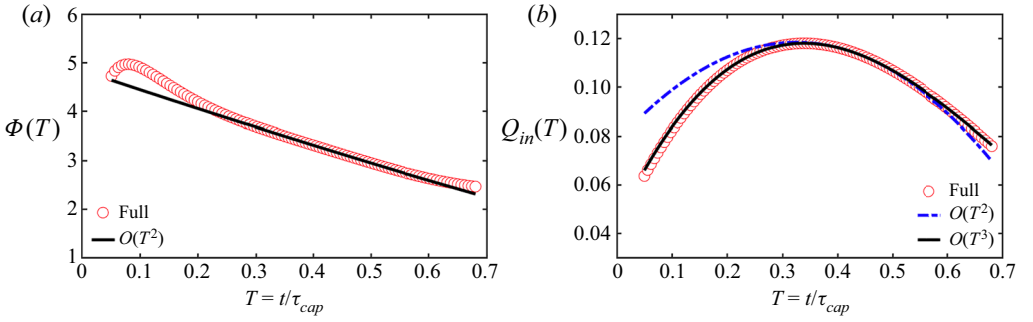

Figure 24. (*a*) Full prediction of the time evolution of the sheet thickness at the rim (A1), compared with its approximate analytic expression (A2). (*b*) Full prediction of the time evolution of the volume rate Q_{in} entering the rim using the full expression (A3), compared with its approximate analytic expression (A4) expanded to different orders.

Funding. This research was supported, in part, by the USDA-NIFA Specialty Crop Research Initiative Grant Award No. MDW-2016-04938, the Richard and Susan Smith Family Foundation and the MIT Ferry Fund. Y.W. is grateful for the partial support of the MIT J.S. Hennessy OGE Fellowship.

Declaration of interest. The authors report no conflict of interest.

Author ORCIDs.
L. Bourouiba https://orcid.org/0000-0001-6025-457X.

Appendix A. Approximate analytic expressions

A.1. *Sheet thickness at the rim*

The sheet thickness $H(R_s, T)$ at the rim in the dimensionless form is derived from

$$H(R_s, T) = \frac{1}{We}\Phi(T) \quad \text{where } \Phi(T) = \frac{\sqrt{6}T}{6a_3F(T)^3 + \sqrt{6}a_2F(T)^2T + a_1F(T)T^2}, \tag{A1}$$

where a_1, a_2 and a_3 are the fixed coefficients of the sheet thickness profile (Wang & Bourouiba 2017). Here, $\Phi(T)$ is the universal evolution function of the sheet thickness at the rim, independent of the impact We. We expand $\Phi(T)$ with a Taylor expansion at the time of maximum radius $T_m = 0.43$ to the order of $O(T^2)$,

$$\left.\begin{aligned} \Phi(T) &= \beta_0 + \beta_1(T - T_m) + \beta_2(T - T_m)^2 \\ \text{with } \beta_i &= \frac{1}{i!}\frac{\mathrm{d}^i}{\mathrm{d}T^i}\Phi(T = T_m), \quad i = 0, 1, 2, \ldots \end{aligned}\right\}, \tag{A2}$$

which gives the values of $\beta_0 = 3.2$, $\beta_1 = -3.6$ and $\beta_2 = 0.36$. Figure 24(*a*) shows the full prediction (A2) as the sheet thickness at the rim is in good agreement with the power series expression (A2) expanded to order $O(T^2)$, which is an order sufficient to capture the full prediction.

A.2. *Volume influx from the sheet to the rim*

The volume influx rate, $Q_{in}(T)$, in (5.11) entering the rim per radian in dimensionless form is

$$Q_{in}(T) = \alpha\sqrt{\Phi(T)}Y_0(T) \quad \text{with } \alpha = \sqrt{\frac{2 - \pi/7}{6}}. \tag{A3}$$

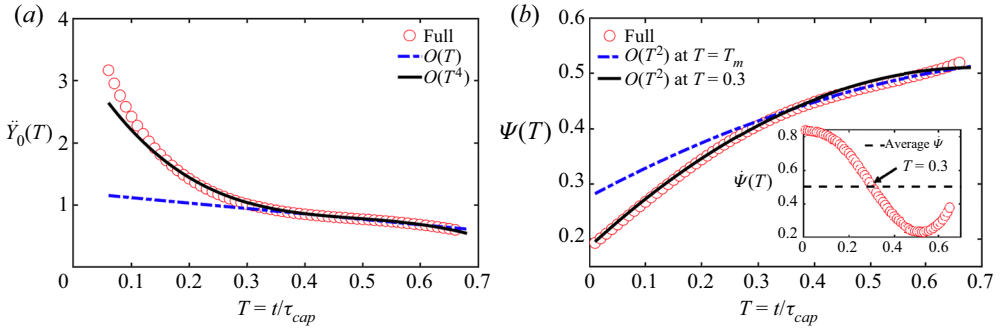

Figure 25. (*a*) Full prediction of the time evolution of the rim deceleration, $\ddot{R}_s$, compared with the approximate analytic expression (A6) expanded at $T_m = 0.43$ to different orders. (*b*) Full prediction of the time evolution of the rim thickness B (A5), compared with the approximate analytical expression (A7) expanded to order $O(T^2)$ around different times. The inset shows the time at which the instantaneous increase rate $\dot{\Psi}(T)$ of the rim thickness is equal to its time-averaged value.

The approximate power series expression of $Q_{in}(T)$ via Taylor expansion of (A3) at the time of maximum radius $T_m = 0.43$ gives

$$\left.\begin{aligned} Q_{in}(T) &= m_0 + m_1(T - T_m) + m_2(T - T_m)^2 + m_3(T - T_m)^3 \\ \text{with } m_i &= \frac{1}{i!}\frac{\mathrm{d}^i}{\mathrm{d}T^i}Q_{in}(T = T_m), \quad i = 0, 1, 2, 3\ldots \end{aligned}\right\}, \tag{A4}$$

which gives the values of $m_0 = 0.11$, $m_1 = -0.08$, $m_2 = 0.38$ and $m_3 = 0.42$. Figure 24(*b*) shows the prediction of the time evolution of the volume rate Q_{in} entering the rim using the full expression (A3), compared with the approximate analytical expression (A4). Note that the data are well captured only with the $O(T^3)$ expansion and not with the $O(T^2)$.

A.3. *Rim thickness and its volume*

Based on the $Bo = 1$ criterion, the rim thickness $B(T)$ in dimensionless form is

$$B = \frac{1}{We^{1/4}}\Psi(T) \quad \text{with } \Psi(T) = [-6\ddot{Y}_0(T)]^{-1/2}, \tag{A5}$$

which is fully determined by the rim deceleration $\ddot{R}_s(T)$. With the original expression of the sheet radius, which is expanded to the order of $O(T^3)$, the expression of the sheet acceleration only has terms on the order of $O(T)$, namely,

$$\frac{\ddot{R}_s}{\sqrt{We}} = \ddot{Y}_0(T) = 6b_3(T - T_m) + 2b_2, \tag{A6}$$

where $b_3 = 0.15$ and $b_2 = -0.41$ are given by (3.8). Figure 25(*a*) shows that the approximate analytic expression (A6) captures the full prediction of the normalized rim acceleration $\ddot{Y}_0$ at later time, but largely deviates from the full solution at early time. In fact, the power series expansion of $\ddot{Y}_0$ has to be expanded at $T = T_m$ to order $O(T^4)$ to capture the full prediction (solid line in figure 25*a*).

For the rim thickness $\Psi(T)$, the situation improves if we take its expansion at another time. The full solution of the rim thickness shows that the rim thickness increases

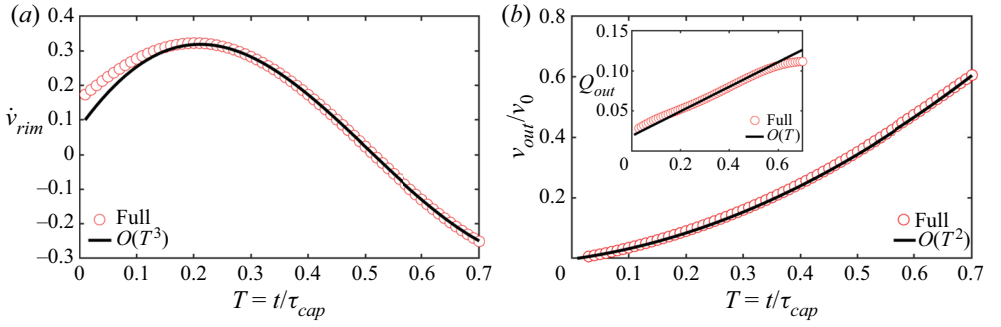

Figure 26. (*a*) Full prediction of the time evolution of the rate of change of rim's volume $\dot{\mathcal{V}}_{rim}$, compared with the approximate analytic expression (A9). (*b*) Full prediction of the time evolution of the volume rate, Q_{out}, (inset) and fraction of cumulative volume, $\mathcal{V}_{out}/\mathcal{V}_0$, shed from the rim, compared with their approximate analytic expressions (A11) and (A12).

over time. To obtain an accurate approximate solution with a low-order expansion, we take the expansion at a time where the instantaneous increase rate of the rim thickness is equal to the time-averaged increase rate, which is around $T = 0.3$ (figure 25*b*-inset). Taking a Taylor expansion (A5) at $T = 0.3$ gives a power series expression of the rim thickness as

$$\left.\begin{aligned} \Psi(T) &= c_0 + c_1(T-0.3) + c_2(T-0.3)^2 \\ \text{with } c_i &= \frac{1}{i!}\frac{\mathrm{d}^i}{\mathrm{d}T^i}\Psi(T=0.3), \quad i = 0, 1, 2\ldots \end{aligned}\right\}, \tag{A7}$$

which gives the values $c_0 = 0.4$, $c_1 = 0.54$ and $c_2 = -0.68$ derived, not fitted. Figure 25(*b*) shows that the power series expansion at $T = 0.3$ to order $O(T^2)$ is sufficient to capture the full prediction, compared with the expansion at $T_m = 0.43$ at the same order.

Based on the rim thickness $B(T)$ and sheet radius $R_s(T)$, the rate of change of rim's volume per radian $\mathcal{V}_{rim}$ is expressed by

$$\dot{\mathcal{V}}_{rim} = \frac{\mathrm{d}}{\mathrm{d}T}\left[\frac{\pi^2}{4}R_s(T)B^2(T)\right] = \frac{\mathrm{d}}{\mathrm{d}T}\left[\frac{\pi^2}{4}Y_0(T)\Psi^2(T)\right]. \tag{A8}$$

Taking a Taylor expansion (A8) at $T_m = 0.43$ gives a power series expression of the rate of change of rim's volume as

$$\dot{\mathcal{V}}_{rim} = \frac{\pi^2}{4}[n_1 + n_2(T-T_m) + n_3(T-T_m)^2 + n_4(T-T_m)^3]. \tag{A9}$$

Using (3.8) and (A7), we can derive the values $n_1 = 0.05$, $n_2 = -0.6$, $n_3 = -0.6$ and $n_4 = 2.52$. Figure 26(*b*) shows that the power series expansion (A9) captures the full solution of $\dot{\mathcal{V}}_{rim}$ very well.

A.4. *Volume outflux shed from the rim*

With the volume influx Q_{in} entering the rim and the rate of change of the rim volume $\mathcal{V}_{rim}$, the volume outflux Q_{out} shed from the rim per radian in non-dimensional form is

$$Q_{out} = \alpha\sqrt{\Phi(T)}\Phi(T) + \frac{\pi}{4}\frac{\mathrm{d}}{\mathrm{d}T}[\Phi(T)\Psi^2(T)] \quad \text{with } \alpha = \sqrt{\frac{2-\pi/7}{6}}. \tag{A10}$$

The full prediction (figure 9*a*) shows that $Q_{out}(T)$ increases with time at an approximate constant rate. Thus, it is sufficient to approximate Q_{out}, to first order, as

$$Q_{out} = p_0 + p_1(T - T_m). \tag{A11}$$

Using power series of Q_{in} and $\dot{\mathcal{V}}_{rim}$ as given by (A4) and (A9), respectively, we can directly derive $p_0 = 0.09$ and $p_1 = 0.15$. The inset of Figure 26(*b*) shows that (A11) captures the full prediction (A10) well.

Taking the integral of (A11) over time T, the fraction of cumulative volume shed from the rim gives

$$\frac{\mathcal{V}_{out}}{\mathcal{V}_0} = 12\int_0^{T'} Q_{out}(T')\,\mathrm{d}T' = 12p_0(T - T_m) + 6p_1(T - T_m)^2. \tag{A12}$$

Figure 26(*b*) shows that the power series expression, (A12), captures the full solution very well.

Appendix B. Mathematical derivations for the energy analysis

B.1. *Energy conservation in the sheet*

For the sheet in the air, taking it to be a 2-D horizontal slender-body, Wang & Bourouiba (2022) derived the unified velocity, $u(r, t)$, and thickness, $h(r, t)$, profiles that satisfy the mass and momentum conservations of the sheet. Without loss of generality, taking the control volume of an annulus between the radial positions r and $r + dr$ in the sheet, the mass and momentum conservations can be expressed in differential form as

$$\left.\begin{array}{c} \dfrac{\partial}{\partial t}(\rho h r) + \dfrac{\partial}{\partial r}(\rho h u r) = 0 \\ \dfrac{\partial}{\partial t}(\rho h u r) + \dfrac{\partial}{\partial r}(\rho h u^2 r) = 0 \longrightarrow \dfrac{\partial u}{\partial t} + u\dfrac{\partial u}{\partial r} = 0 \end{array}\right\}, \tag{B1}$$

where the first term in each equation is the rate of change of mass and momentum per radian in the control volume and the second term in each equation is the net outflux of mass and momentum across the control volume. The unified velocity and thickness profiles of the sheet (Wang & Bourouiba 2017) are solutions of these two equations. To examine whether the energy is conserved in the sheet, consider its rate of change in the control volume:

$$I_1 = \frac{\partial}{\partial t}\left(\frac{1}{2}\rho h u^2 r\right) = \frac{1}{2}\left[u\frac{\partial}{\partial t}(\rho h u r) + \rho h u r\frac{\partial u}{\partial t}\right], \tag{B2}$$

while the net outflux of energy across the control volume is

$$I_2 = \frac{\partial}{\partial r}\left(\frac{1}{2}\rho h u^3 r\right) = \frac{1}{2}\left[u\frac{\partial}{\partial r}(\rho h u^2 r) + \rho h u^2 r\frac{\partial u}{\partial r}\right]. \tag{B3}$$

Adding (B2) with (B3) gives

$$I_1 + I_2 = \frac{1}{2}u\left[\frac{\partial}{\partial t}(\rho h u r) + \frac{\partial}{\partial r}(\rho h u^2 r)\right] + \frac{1}{2}\rho h u r\left(\frac{\partial u}{\partial t} + u\frac{\partial u}{\partial r}\right) = 0, \tag{B4}$$

where the second equality holds based on momentum balance (B1). This indicates that the energy is conserved in the sheet.

B.2. *Proof of energy loss in the rim from momentum balance at the rim*

Here, we consider the case without fluid shedding from the rim. In this case, we can use the analogy of a mass–spring system, where the rim is the mass and the sheet is the spring, with the capillary force as the restoring force. In this analogy, the surface energy of the sheet is the equivalent potential energy of the restoring force. Considering mass and energy conservations reads

$$\left.\begin{aligned} \frac{\mathrm{d}m}{\mathrm{d}t} &= \rho(2\pi r_s)h(r_s,t)[u(r_s,t)-r_s], \\ \frac{\mathrm{d}}{\mathrm{d}t}\left[\frac{1}{2}m(\dot{r}_s)^2+2\sigma(\pi r_s^2)\right] &= \frac{1}{2}\rho(2\pi r_s)h(r_s,t)[u(r_s,t)-r_s]u^2(r_s,t), \end{aligned}\right\} \tag{B5}$$

where $m(t)$ is the rim mass. The first term in the parentheses on the left-hand side of the second equation is the kinetic energy of the rim, while the second term is the surface energy of the sheet – the potential energy of the restoring capillary force. Distinct from the simple spring–mass system, the sheet also continuously injects energy into the rim, which is accounted for with the term on the right-hand side of the second equation.

Now, if we return to the momentum balance at the rim without shedding, it reads

$$\frac{\mathrm{d}}{\mathrm{d}t}(m\dot{r}_s) = \rho(2\pi r_s)h(r_s,t)[u(r_s,t)-r_s]u(r_s,t) - 4\pi\sigma r_s, \tag{B6}$$

where the term on the left-hand side is the rate of change of the rim's momentum. The first term on the right-hand side is the momentum entering the rim per unit of time. The second term is the surface tension force acting on the rim. The energy equation, corresponding to this momentum balance at the rim, can be explored by multiplying both sides of (B6) by $\dot{r}_s$ and re-arranging to read

$$\frac{\mathrm{d}}{\mathrm{d}t}\left[\frac{1}{2}m(\dot{r}_s)^2+2\pi\sigma r_s^2\right] + \frac{1}{2}\dot{m}(\dot{r}_s)^2 = \rho(2\pi r_s)h(r_s,t)[u(r_s,t)-r_s]u(r_s,t)\dot{r}_s. \tag{B7}$$

The factor for the $\dot{r}_s$ term on the right-hand side of (B7) can be simplified using

$$\dot{r}_s = \tfrac{1}{2}u(r_s,t) - \tfrac{1}{2}u(r_s,t) + \dot{r}_s = \tfrac{1}{2}u(r_s,t) - \tfrac{1}{2}[u(r_s,t)-\dot{r}_s] + \tfrac{1}{2}\dot{r}_s, \tag{B8}$$

which leads to a modified balance equation of (B7),

$$\frac{\mathrm{d}}{\mathrm{d}t}\left[\frac{1}{2}m(\dot{r}_s)^2+2\pi\sigma r_s^2\right] + \underbrace{\frac{1}{2}\dot{m}[u(r_s,t)-\dot{r}_s]^2}_{\dot{e}_{ls}} = \frac{1}{2}\rho(2\pi r_s)h(r_s,t)[u(r_s,t)-r_s]u^2(r_s,t), \tag{B9}$$

where mass conservation in (B5) was used.

Compared with the energy conservation equation (B5), the additional term in (B9) from the momentum balance equation is an energy loss term:

$$\dot{e}_{ls} = \tfrac{1}{2}\dot{m}[u(r_s,t)-\dot{r}_s]^2 \quad \text{with } \dot{m} = \rho(2\pi r_s)h(r_s,t)[u(r_s,t)-r_s], \tag{B10}$$

which is positive since $\dot{m} > 0$ as the fluid continuously enters the rim from the sheet in both extension and retraction.

References

Agbaglah, G., Josserand, C. & Zaleski, S. 2013 Longitudinal instability of a liquid rim. *Phys. Fluids* **25** (2), 022103.

Bourouiba, L. 2021*a* The fluid dynamics of disease transmission. *Annu. Rev. Fluid Mech.* **53**, 473–508.

Bourouiba, L. 2021*b* Fluid dynamics of respiratory infectious diseases. *Ann. Rev. Biomed. Engg* **23**, 547–577.

Bourouiba, L., Dehandschoewercker, E. & Bush, J.W.M. 2014 Violent expiratory events: on coughing and sneezing. *J. Fluid Mech.* **745**, 537–563.

Bush, J.W.M. & Aristoff, J.M. 2003 The influence of surface tension on the circular hydraulic jump. *J. Fluid Mech.* **489**, 229–238.

Clanet, C., Béguin, C., Richard, D. & Quéré, D. 2004 Maximal deformation of an impacting drop. *J. Fluid Mech.* **517**, 199–208.

Clanet, C. & Villermaux, E. 2002 Life of a smooth liquid sheet. *J. Fluid Mech.* **462**, 307–340.

Culick, F.E.C. 1960 Comments on a ruptured soap film. *J. Appl. Phys.* **31**, 1128–1129.

Eggers, J., Fontelos, M.A., Josserand, C. & Zaleski, S. 2010 Drop dynamics after impact on a solid wall: theory and simulations. *Phys. Fluids* **22**, 062101.

Gilet, T. & Bourouiba, L. 2014 Rain-induced ejection of pathogens from leaves: revisiting the hypothesis of splash-on-film using high-speed visualization. *Integr. Compar. Biol.* **54**, 974–84.

Gilet, T. & Bourouiba, L. 2015 Fluid fragmentation shapes rain-induced foliar disease transmission. *J. R. Soc. Interface* **12**, 20141092.

Gordillo, J.M., Lhuissier, H. & Villermaux, E. 2014 On the cusps bordering liquid sheets. *J. Fluid Mech.* **754**, R1.

Josserand, C. & Thoroddsen, S.T. 2016 Drop impact on a solid surface. *Annu. Rev. Fluid Mech.* **48**, 365–391.

Krechetnikov, R. & Homsy, G.M. 2009 Crown-forming instability phenomena in the drop splash problem. *J. Colloid Interface Sci.* **331** (2), 555–559.

Lagubeau, G., Fontelos, M.A., Josserand, C., Maurel, A., Pagneux, V. & Petitjeans, P. 2012 Spreading dynamics of drop impacts. *J. Fluid Mech.* **713**, 50–60.

Lee, J.B., Laan, N., de Bruin, K.G., Skantzaris, G., Shahidzadeh, N., Derome, D., Carmeliet, J. & Bonn, D. 2016 Universal rescaling of drop impact on smooth and rough surfaces. *J. Fluid Mech.* **786**, R4.

Lejeune, S., Gilet, T. & Bourouiba, L. 2018 Edge effect: liquid sheet and droplets formed by drop impact close to an edge. *Phys. Rev. Fluids* **3**, 083601.

Néel, B., Lhuissier, H. & Villermaux, E. 2020 'Fines' from the collision of liquid rims. *J. Fluid Mech.* **893**, A16.

Peters, I.R., van der Meer, D. & Gordillo, J.M. 2013 Splash wave and crown breakup after disc impact on a liquid surface. *J. Fluid Mech.* **724**, 553–580.

Rein, M. 1993 Phenomena of liquid drop impact on solid and liquid surfaces. *Fluid Dyn. Res.* **12**, 61–93.

Riboux, G. & Gordillo, J.M. 2015 The diameters and velocities of the droplets ejected after splashing. *J. Fluid Mech.* **772**, 630–648.

Riboux, G. & Gordillo, J.M. 2016 Maximum drop radius and critical Weber number for splashing in the dynamical Leidenfrost regime. *J. Fluid Mech.* **803**, 516–527.

Roisman, I.V., Berberovi, E. & Tropea, C. 2009 Inertia dominated drop collisions. I. On the universal flow in the lamella. *Phys. Fluids* **21**, 052103.

Roisman, I.V., Horvat, K. & Tropea, C. 2006 Spray impact: rim transverse instability initiating fingering and splash, and description of a secondary spray. *Phys. Fluids* **18**, 102104.

Roisman, I.V. & Tropea, C. 2002 Impact of a drop onto a wetted wall: description of crown formation and propagation. *J. Fluid Mech.* **472**, 373–397.

Rozhkov, A., Prunet-Foch, B. & Vignes-Adler, M. 2002 Impact of water drops on small targets. *Phys. Fluids* **14**, 3485.

Rozhkov, A., Prunet-Foch, B. & Vignes-Adler, M. 2004 Dynamics of a liquid lamella resulting from the impact of a water drop on a small target. *Proc. R. Soc. Lond.* A **460**, 2681–2704.

Savart, F. 1833 Mémoire sur le choc de deux veines liquides animées de mouvements directement opposés. *Ann. Chim.* **55**, 257–310.

Taylor, G.I. 1959 The dynamics of thin sheet of fluids. II. Waves on fluid sheets. *Proc. R. Soc. Lond.* A **253**, 289–312.

Traverso, G., Laken, S., Lu, C.C., Maa, R., Langer, R. & Bourouiba, L. 2013 Fluid fragmentation from hospital toilets. e-prints. arXiv:1310.5511.

VERNAY, C., RAMOS, L. & LIGOURE, C. 2015 Free radially expanding liquid sheet in air: time- and space-resolved measurement of the thickness field. *J. Fluid Mech.* **764**, 428–444.

VILLERMAUX, E. & BOSSA, B. 2011 Drop fragmentation on impact. *J. Fluid Mech.* **668**, 412–435.

WANG, Y. & BOUROUIBA, L. 2017 Drop impact on small surfaces: thickness and velocity profiles of the expanding sheet in the air. *J. Fluid Mech.* **814**, 510–534.

WANG, Y. & BOUROUIBA, L. 2018*a* Non-isolated drop impact on surfaces. *J. Fluid Mech.* **835**, 24–44.

WANG, Y. & BOUROUIBA, L. 2018*b* Unsteady sheet fragmentation: droplet sizes and speeds. *J. Fluid Mech.* **848**, 946–967.

WANG, Y. & BOUROUIBA, L. 2021 Growth and breakup of ligaments in unsteady fragmentation. *J. Fluid Mech.* **910**, A39.

WANG, Y. & BOUROUIBA, L. 2022 Non-Galilean Taylor-Culick's law governs sheet dynamics in unsteady fragmentation. *J. Fluid Mech.* (in Press).

WANG, Y., DANDEKAR, R., BUSTOS, N., POULAIN, S. & BOUROUIBA, L. 2018 Universal rim thickness in unsteady sheet fragmentation. *Phys. Rev. Lett.* **120**, 204503.

YARIN, A.L. 2006 Drop impact dynamics: splashing, spreading, receding, bouncing.... *Annu. Rev. Fluid Mech.* **38**, 159–192.

YARIN, A.L. & WEISS, D.A. 1995 Impact of drops on solid surfaces: self-similar capillary waves, and splashing as a new type of kinematic discontinuity. *J. Fluid Mech.* **283**, 141–173.

ZHANG, L.V., BRUNET, P., EGGERS, J. & DEEGAN, R.D. 2010 Wavelength selection in the crown splash. *Phys. Fluids* **22**, 122105.